Handbook of Advanced Ceramics
S. Sōmiya *et al.* (Eds.)

4.1 Sintering of Ceramics

LUTGARD C. DE JONGHE[1] and MOHAMED N. RAHAMAN[2]

[1]*Department of Materials Science and Engineering, University of California at Berkeley, and the Lawrence Berkeley National Laboratory, Materials Sciences Division, Berkeley, CA 94720-1760, USA*
[2]*Department of Ceramic Engineering, University of Missouri-Rolla, Rolla, MO 65409-0330, USA*

4.1.1 INTRODUCTION

Because of the high melting point of the raw materials, the fabrication of ceramics commonly includes a heat treatment step in which a powder, already formed into a required shape, is converted into a dense solid. This step is referred to *sintering* (or *firing*). In general, a ceramist, wishing to produce a material with particular properties, must identify the required microstructure and then design processing conditions that will produce this required microstructure. The objective of sintering studies is therefore commonly to understand how the processing variables such as temperature, particle size, applied pressure, particle packing, composition and sintering atmosphere influence the microstructure that is produced. Several texts have been published in recent years that provide a detailed treatment of the theory, principles, and practice of sintering [1–3]. In the present article, we outline the basic principles of sintering and how they are applied practically to the production of ceramics with controlled microstructures.

There are four categories of sintering which are dependent on the composition being fired and on the extent to which second phases are formed during the heat treatment:

Solid-state sintering: the shaped green body is heated to a temperature that is typically 0.5–0.9 of the melting point. No liquid is present and atomic diffusion in the solid state produces joining of the particles and reduction of the porosity.

Liquid-phase sintering: a small amount of liquid, typically less than a few volume percent of the original solid mixture, is present at the sintering temperature. The liquid volume is insufficient to fill the pore space so that additional processes are required to achieve full densification. Liquid-phase sintering is an important method for the industrial fabrication of many ceramics. While the liquid phase can allow enhanced densification at lower temperatures, a difficulty, particularly in the case of ceramics for structural applications, is that the maximum use temperature of the material may be controlled by the softening temperature of the solidified liquid phase.

Vitrification: for a mixture where a relatively large volume of liquid (typically greater than ~25% of the original solid volume) is formed on heating, the liquid volume is sufficient to fill the volume of the remaining pores. Thus, a dense product can be achieved by the formation of the liquid, flow of the liquid into the pores, and either crystallization or vitrification (glass formation) of the liquid on cooling. Vitrification is particularly important for the production of ceramics from naturally available raw materials such as clays.

Viscous sintering: a consolidated mass of glass particles is heated near to, or above its softening temperature. Densification occurs by viscous flow of the glass under the influence of surface tension.

Under some conditions, densification achieved by any of the four categories of sintering might be inadequate. A solution to this problem is the application of an external pressure during heating, giving the method of *pressure sintering* (of which hot pressing and hot isostatic pressing are common examples). Pressure sintering has the disadvantage of increased fabrication costs but is effective when a microstructure of high density and fine grain size must be guaranteed. To distinguish it from pressure sintering, sintering performed without the application of an external pressure is commonly referred to as *conventional sintering*. A list of some ceramic compositions and the way they are sintered is given in Table 4.1.1.

4.1.2 SOLID-STATE SINTERING

4.1.2.1 DRIVING FORCES

It is generally accepted that the reduction in the surface free energy of a sintering compact, due to the elimination of internal surface area associated with the pores, provides the driving force for sintering. When compared to other processes (e.g. chemical reactions), the decrease in the surface free energy during sintering is rather small (~100 J/mol for particles with an initial diameter of 1 μm) but the distance that matter has to be transported is also small (of the order of the particle size), so that sintering occurs at a reasonable rate at sufficiently high temperatures.

TABLE 4.1.1 Selected Ceramic Compositions and the Sintering Process Used for their Densification

Composition	Sintering process	Application
Al_2O_3	Solid-state sintering with MgO additive	Sodium vapor arc lamp tubes
	Liquid-phase sintering with a silicate glass	Furnace tubes; refractories
MgO	Liquid-phase sintering with a silicate glass	Refractories
Si_3N_4	Liquid-phase sintering with oxide additives (e.g. Al_2O_3 and Y_2O_3) under nitrogen gas pressure or under an externally applied pressure	High-temperature structural ceramics
SiC	Solid-state sintering with B and C additives; liquid-phase sintering with Al, B and C or oxide additives	High-temperature structural ceramics
ZnO	Liquid-phase sintering with Bi_2O_3 and other oxide additives	Electrical varistors
$BaTiO_3$	Liquid-phase sintering with TiO_2-rich liquid	Capacitor dielectrics; thermistors
$Pb(Zr,Ti)O_3$ (PZT), $(Pb,La)(Zr,T)O_3$ (PLZT)	Sintering with a lead-rich liquid phase; hot pressing	Piezoelectric actuators and electro-optic devices
$ZrO_2/(3–10\,mol\%\ Y_2O_3)$	Solid-state sintering	Electrical conducting oxide for fuel cells
Mn–Zn and Ni–Zn ferrites	Solid-state sintering under a controlled oxygen atmosphere	Soft ferrites for magnetic applications
Porcelain	Vitrification	Electrical insulators; tableware
SiO_2 gel	Viscous sintering	Optical devices

The specific energy and curvature of the particle surfaces provide an effective stress on the atoms under the surface. For a curved surface with principal radii of curvature r_1 and r_2, this stress is given by the equation of Young and Laplace:

$$\sigma = \gamma_{sv}\left(\frac{1}{r_1} + \frac{1}{r_2}\right) \tag{1}$$

where γ_{sv} is the specific surface energy. The *diffusion potential*, μ, which drives matter transport is in this case found by equating the mechanical work performed by the stress to the thermodynamic work required for the reduction of the surface free energy. A commonly used relation is

$$\mu = \sigma\Omega \tag{2}$$

where Ω is the atomic or molar volume. The equation for μ is actually more complex for polycrystalline ceramics where the pores are in contact with the grain boundaries [4].[1] For example, in the final stage of sintering where the pores are assumed to be spherical, one expression is [5]:

$$\mu = \Omega\left(\frac{2\gamma_{gb}}{G} + \frac{2\gamma_{sv}}{r}\right) \tag{3}$$

where γ_{gb} is the specific energy of the grain boundary, G is the diameter of the grains, and r is the radius of the pores. According to Eq. 3, the chemical potential consists of two contributions, one attributed to the pores and the other attributed to the boundaries.

A further development is to relate the chemical potential to an externally applied stress. The driving force for sintering is then defined in terms of a *sintering stress*, Σ, which is the *equivalent externally applied stress* that has the same effects on sintering as the curved surfaces of pores and grain boundaries [4]. The formulation of the driving force in terms of a fictitious externally applied stress is advantageous in the analysis of sintering where mechanical stress effects arise (e.g. pressure sintering and constrained sintering). It also provides a conceptual basis for designing experiments to measure the sintering stress (see Section 4.1.2.7).

4.1.2.2 STAGES OF SINTERING

The microstructure of a powder compact, consisting initially of discrete particles, evolves continuously during sintering. However, it is sometimes convenient to divide the process into three idealized stages defined in terms of the microstructure, to force correspondence between simple, established sintering models. The *initial stage* would begin as soon as some degree of atomic mobility is achieved and, during this stage, sharply concave necks form between the individual particles. The amount of densification is small, typically the first 5% of linear shrinkage, and it can be considerably lower if coarsening mechanisms are very active. In the *intermediate stage*, the high curvatures of the initial stage

---

[1] Cannon, R. M. On the effects of dihedral angle and pressure on the driving forces for pore growth or shrinkage, unpublished work.

have been moderated and the microstructure consists of a three-dimensional interpenetrating network of solid particles and continuous, channel-like pores. This stage is considered valid to ~5–10% porosity and therefore covers most of the densification. Grain growth (coarsening) starts to become significant. As sintering proceeds, the channel-like pores break down into isolated, closed voids, which marks the start of the *final stage*. Grain growth can be more extensive in the final stage and difficulties are commonly encountered in the removal of the last few percent of porosity.

4.1.2.3 Mechanisms of Sintering

Sintering of crystalline materials can occur by several mechanisms (i.e. atomic transport paths and their associated sources and sinks): vapor transport (evaporation/condensation), surface diffusion, lattice (volume) diffusion, grain boundary diffusion, and dislocation motion. Figure 4.1.1 shows a schematic representation of the matter transport paths for two sintering particles. A distinction is commonly made between *densifying* and *non-densifying* mechanisms. Vapor transport, surface diffusion, and lattice diffusion from the particle surfaces to the neck lead to neck growth and coarsening of the particles without densification. Grain boundary diffusion and lattice diffusion from the grain boundary to the neck are the most important densifying mechanisms

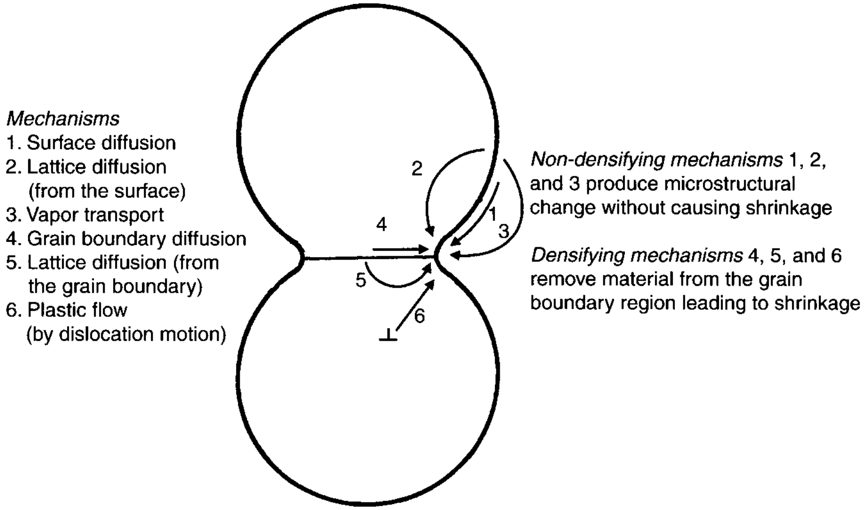

FIGURE 4.1.1 Schematic representation of the sintering mechanisms for a system of two particles.

in polycrystalline ceramics. Diffusion from the grain boundaries to the pores permits neck growth as well as shrinkage (densification). Plastic flow by dislocation motion can cause neck growth and densification through deformation (creep) of the particles in response to the sintering stress. Plastic flow is more common in the sintering of metal powders. For glass powders, which cannot have grain boundaries, densification and neck growth occurs by viscous flow, involving deformation of the particles.

In addition to the alternative mechanisms, there are additional complications arising from the diffusion of the different *ionic species* making up the compound. To preserve charge neutrality of the local composition, the flux of the different ionic species will be coupled [6–8]. A further complication arises because each ionic species can diffuse along different paths. For an oxide with the formula M_xO_y, the effective (*ambipolar*) diffusion coefficient is given by [9]:

$$\bar{D} = \frac{(x+y)[D_l^M + \pi\delta_{gb}D_{gb}^M/G][D_l^O + \pi\delta_{gb}D_{gb}^O/G]}{y[D_l^M + \pi\delta_{gb}D_{gb}^M/G] + x[D_l^O + \pi\delta_{gb}D_{gb}^O/G]} \tag{4}$$

where D is the diffusion coefficient, G is the grain size, δ is the thickness of the grain boundary, the subscripts l and gb refer to lattice and grain boundary diffusion, respectively, and the superscripts M and O refer to the metal and oxygen ions, respectively. According to Eq. 4, whatever the relative magnitudes of the four diffusivities, it is the *slowest diffusing species along its fastest path* that controls the rate. Another complicating factor is that the rate-controlling mechanism for a given material can change with changing conditions of the process variables such as temperature, grain size, and composition [10].

A complicating factor that has been exploited effectively in solid-state sintering is that aliovalent dopants and impurities alter the point defect concentration [11, 12], thereby altering the diffusion coefficients and the sintering rates. For example, the addition of TiO_2 to Al_2O_3 influences the sintering rate in a way that could be explained in terms of the effect of TiO_2 on the concentration of Al vacancies [13]. In general, the effects of dopants on the sintering rates cannot be easily explained because of the multiplicity of the dopant role [14, 15]: for example, influence on more than one diffusion process, segregation at the grain boundaries, influence on surface and grain boundary energies, and the formation of second phases.

4.1.2.4 COMPETITION BETWEEN DENSIFICATION AND COARSENING

The various sintering mechanisms do not operate independently. Vapor transport and surface diffusion compete with the densifying mechanism. They

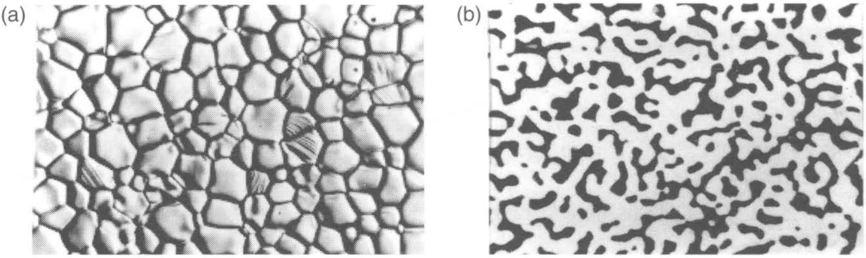

FIGURE 4.1.2 (a) The surface of an Al_2O_3 ceramic from which all porosity has been removed during sintering in which the densifying processes dominate. (b) The sintering of silicon where coarsening mechanisms dominate results in formation of a continuous network of solid material (white) and porosity (black). The microstructural change is not accompanied by any densification. (From Brook, R. J. (1991). *Concise Encyclopedia of Advanced Ceramics*. With kind permission of Elsevier, Oxford.)

lead to coarsening of the microstructure and a reduction of the driving force for sintering, so that a significant reduction in the densification rate can result. Sintering is, therefore, said to involve a competition between densification and coarsening. The production of ceramics with high density (Fig. 4.1.2a) would require choosing the sintering conditions so that the non-densifying mechanisms are not very active (see Section 4.1.7). When coarsening mechanisms dominate, the production of a highly porous body is favored (Fig. 4.1.2b).

4.1.2.5 EFFECTS OF GRAIN BOUNDARIES

In the sintering of polycrystalline materials, part of the energy decrease due to elimination of internal surface area associated with the pores goes into creating new grain boundary area. The grains also have a tendency to grow, by migration of the boundaries, to reduce the energy associated with the grain boundaries, thereby leading to an increase in the diffusion distance. The presence of the grain boundaries also dictates the equilibrium shape of the pores at the intersection with the boundaries. At equilibrium, the chemical potential of the atoms in the pore surface must be the same everywhere, which is equivalent to saying that the curvature of the pore surface is the same everywhere. This means that the pore surface must consist of circular arcs in two-dimensional models, and of spherical caps in a very limited number of three-dimensional geometries, for isotropic solids. There must also be a balance of forces at the junction between the grain boundary and the pore surface. Ignoring possible torque terms, as

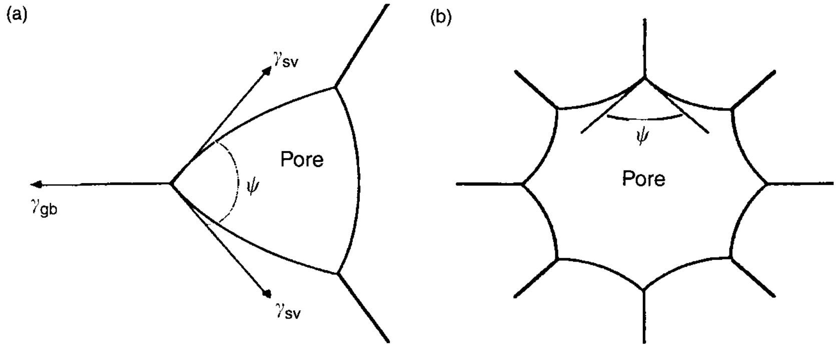

FIGURE 4.1.3 Pore shape and pore stability are determined by the dihedral angle and the pore coordination number: (a) The pore with the concave surfaces will shrink while (b) the pore with the convex surfaces will grow (or become metastable).

shown in Figure 4.1.3a this balance of forces leads to

$$\cos\left(\frac{\psi}{2}\right) = \frac{\gamma_{gb}}{2\gamma_{sv}} \tag{5}$$

where ψ is the dihedral angle, γ_{gb} is the specific grain boundary energy, and γ_{sv} is the specific surface energy.

The pore surface in Figure 4.1.3a is concave (negative curvature) and during sintering, the surface will move towards its center of curvature, so that the pore will shrink. However, as shown in Figure 4.1.3b, when the pore is surrounded by a large number of grains (i.e. the *pore coordination number* is large), the balance of forces at the grain boundary/pore junction dictates that the pore surface will become convex (positive curvature). In this case the pore will grow or become metastable (R. M. Cannon, unpublished work). Whether or not pores can shrink in a powder compact has been analyzed in thermodynamic terms by Kingery and François [16]. The balance between the reduction in pore surface area and the increase in the grain boundary area leads to a criterion that prescribes the maximum pore coordination number that will permit a pore to shrink. As shown in Figure 4.1.4, for a given dihedral angle (e.g. 120°), pores with a coordination number less than a certain critical value, ($N_c = 12$), will shrink while pores with $N > N_c$ will grow. The large pores in a powder compact will have large values of N and will therefore be difficult to shrink, leading to residual porosity in the sintered material. The importance of controlling particle packing for the achievement of high density is therefore clear.

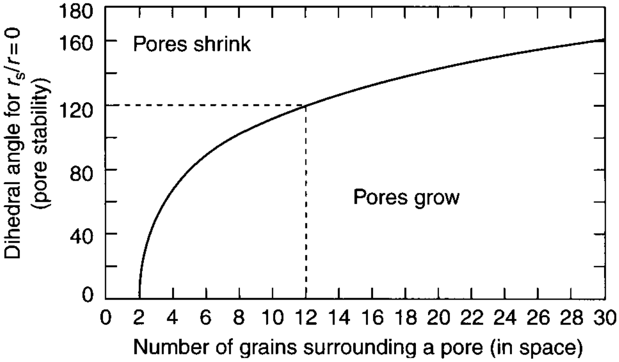

FIGURE 4.1.4 Conditions for pore stability as a function of pore coordination number and dihedral angle. For a dihedral angle of 120°, pores surrounded by more than 12 grains will grow (from Ref. [16]).

4.1.2.6 SINTERING MODELS

Matter transport during sintering is driven by chemical potential gradients arising from differences in the curvature of the free surfaces in the compact of particles. When compared to atoms under a flat surface at the same temperature and composition, the atoms under a convex surface have a higher chemical potential while the atoms under a concave surface have a lower chemical potential. This gradient in the chemical potential produces a driving force for matter transport from the (convex) particle surfaces and from the grain boundaries between the particles to the (concave) necks between the particles (Figure 4.1.1). Mathematical models have been developed to analyze the rate of matter transport along these paths. The models can be classified into three types: (a) analytical models; (b) scaling laws; and (c) numerical models.

4.1.2.6.1 Analytical Models

The analytical models assume a simplified, highly idealized geometry for each stage of sintering and, for each mechanism, the diffusional flux equations are solved analytically to provide equations for the sintering kinetics. They have often been criticized for their simplified and generalized assumptions about the microstructure of the sintering compact (e.g. monodisperse particles, uniform packing, generalized grain and pore shapes, absence of grain growth). However, they are useful for providing an excellent *qualitative* understanding of sintering in terms of the driving force, the mechanisms and the influence of primary variables (e.g. particle size, temperature, applied pressure, heating rate, atmosphere).

For the two-sphere geometry assumed for the initial stage (Fig. 4.1.1), equations for neck growth (and shrinkage for the densifying mechanisms) have been derived for each mechanism and are summarized elsewhere [2, 17, 18]. The initial-stage equations played a key role in the early development of sintering theory but their usefulness in practical sintering is quite limited. For the intermediate and final stages of sintering, Coble [19–21] assumed the grain shape to be a tetrakaidecahedron and derived equations for conventional sintering by lattice and grain boundary diffusion, and for sintering with an applied pressure. The most useful feature of the sintering equations is the predicted dependence of the densification rate on the primary processing variables. For any stage of the sintering process, the model predictions for the densification rate, $\dot{\varepsilon}_\rho = (1/\rho)\,\mathrm{d}\rho/\mathrm{d}t$, can be expressed in general form [1, 2]:

$$\dot{\varepsilon}_\rho = \left(\frac{1}{\rho}\right)\frac{\mathrm{d}\rho}{\mathrm{d}t} = \frac{HD\Omega\phi^{(m+1)/2}}{G^m kT}(p_\mathrm{a} + \Sigma) \tag{6}$$

where H is a numerical constant that depends on the assumed geometry of the model and on the sintering mechanism, Ω is the atomic volume of the rate controlling species, G is the grain (or particle) size, k is the Boltzmann constant, and T is the absolute temperature. The diffusion coefficient D and the grain size exponent, m, take on their appropriate values for a given mechanism: $D = D_\mathrm{l}$ and $m = 2$ for lattice diffusion, where D_l is the lattice diffusion coefficient; $D = D_\mathrm{gb}\delta_\mathrm{gb}$ and $m = 3$ for grain boundary diffusion, where δ_gb is the grain boundary thickness. The term Σ is the sintering stress, defined earlier as the *equivalent externally applied stress* that has the same effects on sintering as the curved surfaces of pores and grain boundaries. The term ϕ, referred to as the *stress intensification factor*, is a geometrical parameter that relates the externally applied stress to the actual stress on the grain boundaries (see Sections 4.1.2.7 and 4.1.2.8). For diffusional mass transport, Eq. 6 predicts that for an equivalent microstructure, the densification rate increases almost exponentially with T (due to the strong Arrhenius dependence of D on T), increases linearly with the applied pressure, p_a, and has a strong dependence on G. For reasonably homogeneous particle packing and under conditions when grain growth is limited (e.g. during hot pressing under a significant stress), these predictions have been verified by experiments. In conventional sintering, while the benefits of small particle size are significant, the measured densification rates are considerably lower than the predicted values because of inhomogeneous particle packing and the inevitable coarsening processes (see Section 4.1.7.3).

4.1.2.6.2 Herring's Scaling Law

Herrings scaling law [22] does not assume a specific geometrical model. Instead, it assumes that the geometrical changes remain similar. The law considers the effect of change of scale (e.g. particle size) on the rate of matter transport for individual mechanisms. The times for equivalent geometric change can be expressed as:

$$\frac{t_2}{t_1} = \left(\frac{G_{2,0}}{G_{1,0}}\right)^m \tag{7}$$

where the subscripts 1 and 2 represent two different powders with initial particle size $G_{1,0}$ and $G_{2,0}$, respectively and m is an integer that depends on the mechanism of matter transport: $m = 4$ for surface diffusion and for grain boundary diffusion, $m = 2$ for vapor transport, and $m = 3$ for lattice diffusion. For an equivalent geometrical change, the law states that the rate of sintering varies as $1/G^m$. Since the densification rate varies as $1/G^4$ for grain boundary diffusion and as $1/G^3$ for lattice diffusion, the grain boundary path is favored for fine particles. The rate of coarsening by surface diffusion also varies as $1/G^4$ so that grain boundary diffusion and surface diffusion are expected to be in competition during the sintering of fine particles. Because of the general approach used in its derivation, the scaling law might be expected to have some advantage over the analytical models that assume a specific geometry. A problem is that the requirement of geometrically similar microstructural change is not easy to achieve for real powder compacts and the law has not found any significant applicability in sintering [23].

4.1.2.6.3 Numerical Modeling

In practice, more than one mechanism operates during sintering. While sintering with *concurrent mechanisms* has been treated by the analytical models [24], the problem is better solved by numerical simulations that allow the use of more realistic geometries [25, 26]. In particular, finite-element modeling has been used very effectively in the analysis of a variety of sintering problems [27–29]. The calculations can be fairly complex, which may be a reason why the approach has not yet achieved much popularity.

4.1.2.6.4 Sintering Maps

Sintering maps have been constructed to show the dominant mechanisms as functions of the temperature and density [30, 31]. The construction employs the sintering equations derived in the analytical models and data for the material parameters in the equations. Because of the inadequacy of the database and the drastic simplifications of the models, the applicability of the maps is limited.

Nevertheless, they have proved useful in visualizing conceptual relationships between the various mechanisms and changes in the sintering behavior under different sintering conditions.

4.1.2.7 THE SINTERING STRESS

The formulation of the driving force for sintering, the *sintering stress*, in terms of an equivalent external stress, as outlined earlier, provides a conceptual basis for designing experiments to measure the sintering stress. Gregg and Rhines [32] used a *zero creep* experiment in which the externally applied stress required to counteract the shrinkage of the compact due to sintering was determined. De Jonghe and coworkers [33–37] developed the technique of loading dilatometry, in which a small, controlled uniaxial stress is applied to the sintering compact. Measurement of the time-dependent axial and radial strains allows the determination of the volumetric (densification) strain rate and the creep strain rate. Venkatachari and Raj [38] used a sinter-forging technique in which considerably higher uniaxial stresses were applied.

In the loading dilatometry experiments, the hydrostatic component of the applied uniaxial stress is small compared to the sintering stress, so that the sintering mechanism of the loaded powder compact is expected to be identical to that for a freely sintered compact. Equation 6 can be written as [1, 2]

$$\dot{\varepsilon}_\rho = \frac{HD\Omega\phi^{(m+1)/2}}{G^m kT}\Sigma \tag{8}$$

Assuming the same mechanism for creep under the low uniaxial stress, p_z, an equation for the creep rate is

$$\dot{\varepsilon}_c = \frac{H'D\Omega\phi^{(m+1)/2}}{G^m kT}p_z \tag{9}$$

where H' is a numerical constant. The ratio of the densification rate to the creep rate can be found from Eqs 8 and 9 as

$$\frac{\dot{\varepsilon}_\rho}{\dot{\varepsilon}_c} = \frac{F\Sigma}{p_z} \tag{10}$$

where F is a constant. Measurement of the densification rate and the creep rate at a fixed value of p_z for identical samples indicates that the ratio $\dot{\varepsilon}_\rho/\dot{\varepsilon}_c$ is fairly constant over a wide density range for several materials (Fig. 4.1.5).

Making reasonable assumptions for the value of F, the value of Σ can be determined from Eq. 6 using the measured values of $\dot{\varepsilon}_\rho/\dot{\varepsilon}_c$ and p_z [34]. The sintering stress determined in this way is shown in Figure 4.1.6 for CdO. It is of

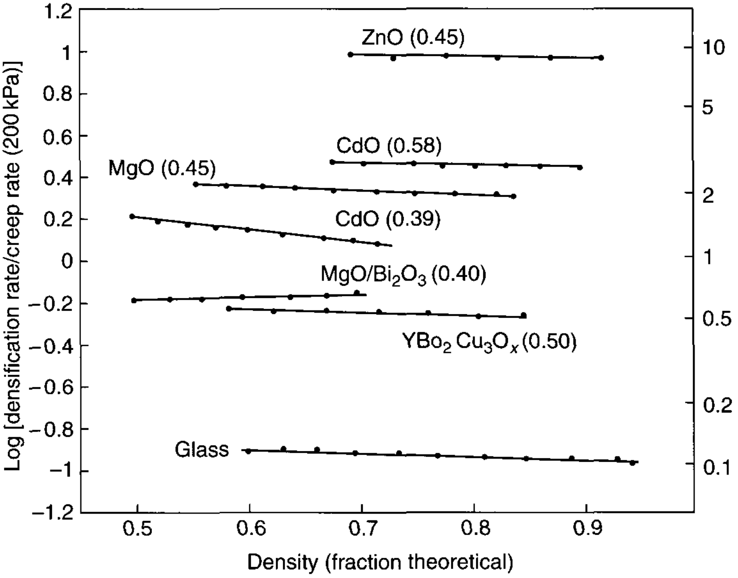

FIGURE 4.1.5 The ratio of the densification rate to the creep rate at a constant stress (0.2 MPa) for various ceramics and for glass. The numbers in parentheses are the initial densities (from Ref. [36]).

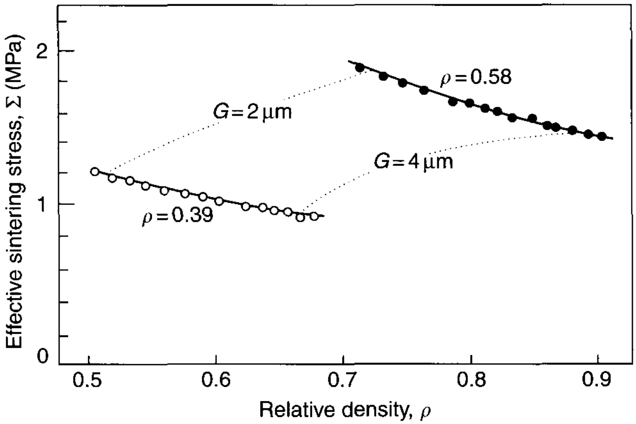

FIGURE 4.1.6 Sintering stress versus relative density for CdO powder compacts of two different initial densities ρ (from Ref. [34]).

the order of 1–2 MPa and, for a given green density, appears to be relatively constant over a large part of the densification process. Based on the sintering model of Coble [21], it might be expected that Σ would increase with densification after the initial stage of sintering. The observed decrease may have its origins in processes such as differential densification and coarsening that are not taken into account in the models. In fact, the sintering stress of Cu powder compacts measured by Gregg and Rhines [32] increased with densification up to ~95% of the theoretical density, after which it decreased due presumably to coarsening [39]. A decrease in Σ with initial density, seen in Figure 4.1.6, has also been observed for ZnO [37]. At a given density, Σ is also expected to vary inversely as the particle (or grain) size but this has not been studied in experiments of the type described here.

4.1.2.8 THE STRESS INTENSIFICATION FACTOR

Solid-state sintering involves atomic transport from the grain boundaries to fill up the pores and is dependent on the *effective stress* on the grain boundaries. We therefore require a way to relate the externally applied stress, σ_a, to the effective stress on the grain boundary, σ_e. This has been commonly achieved (see Eq. 6) by using a parameter, ϕ, referred to as the *stress intensification factor*, that depends on the geometry of the porous compact:

$$\sigma_e = \sigma_a \phi \tag{11}$$

The stress intensification factor is equal to the ratio of the total cross-sectional area (of the solid phase plus the pores), A_t, to the effective cross-sectional area (of the solid-phase only), A_e. For a polycrystalline material, ϕ is equal to the cross-sectional area of the grain, A_g, divided by the grain boundary area, A_{gb}:

$$\phi = \frac{A_t}{A_e} = \frac{A_g}{A_{gb}} \tag{12}$$

If the pores are spherical and randomly distributed through the porous compact, such as a glass in the final stage of sintering, ϕ takes a simple form [21]:

$$\phi = 1/\rho \tag{13}$$

where ρ is the relative density of the compact. In general, the relationship may be expected to be complex. However, computer calculations by Beere [40] on the equilibrium shapes of pores in a porous compact yield results that can be well fitted to simple analytical expressions. One expression is [41]

$$\phi = \exp[a(1 - \rho)] \tag{14}$$

where a is a constant that depends on the dihedral angle of the pores (Fig. 4.1.2). Data for the creep rates of some porous compacts measured in the loading dilatometry experiments described earlier [34, 35] yield values for ϕ that can be well fitted by Eq. 14. An example of such data is shown in Figure 4.1.7 for CdO.

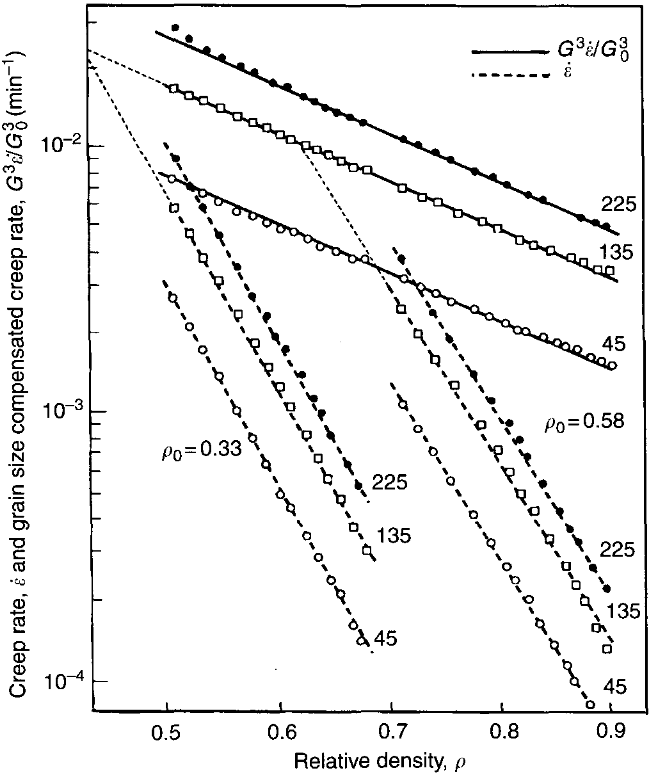

FIGURE 4.1.7 Dependence of the creep rate and the grain size compensated creep rate of CdO powder compacts on relative density for compacts with initial densities of 0.39 and 0.58 subjected to uniaxial stress shown in kPa (from Ref. [34]).

4.1.3 GRAIN GROWTH AND COARSENING

Grain growth is the term used to describe the increase in the average grain size of a polycrystalline material. The grain boundary is a region with a complex structure, about 1–2 unit cells wide, between two crystalline domains. It has a higher energy than the bulk crystal and, hence, a reduction in the grain boundary area will reduce the free energy of the system. The grain boundary moves by diffusion of atoms (ions) from one side of the boundary to the other so that atoms previously aligned with one grain becomes aligned with the other, causing it to grow at the expense of its neighbor. Growth occurs in such a way that the convex grain loses atoms while the concave grain gains atoms with the result that the boundary moves towards its center of curvature.

The term *coarsening* is frequently used to describe the process in porous ceramics whereby the increase in the average grain size is accompanied by an increase in the average pore size. Coarsening, as we have observed, reduces the driving force for sintering and increases the diffusion distance for matter transport, thereby reducing the rate of sintering. The suppression of coarsening mechanisms therefore forms a key requirement for the achievement of high density. Another requirement is that the microstructure be stabilized such that the pores and the grain boundaries remain attached. This second requirement depends primarily on the ability to reduce the intrinsic (pore-free) mobility of the grain boundaries. An understanding of grain growth in dense ceramics therefore forms a key step towards controlling grain growth during the sintering of powder compacts.

Coarsening of precipitates or particles in a solid, liquid, or gaseous medium is commonly referred to as *Ostwald ripening*. It is especially important in liquid-phase sintering where matter transport driven by chemical potential differences causes the smaller grains to become smaller and the larger particles to grow, resulting in an increase in the average grain size. Many features of coarsening (pore growth and grain growth) in solid-state sintering are also shared by the Ostwald ripening process.

Grain growth in ceramics is generally divided into two types: (i) *normal* grain growth and (ii) *abnormal* grain growth, which is sometimes referred to as *exaggerated grain growth* or *discontinuous grain growth*. In normal grain growth, the average grain size increases with time but the grain size distribution remains self-similar (invariant in time). Abnormal grain growth is the process whereby a few large grains grow rapidly at the expense of the smaller grains, giving a bimodal grain size distribution. *Anisotropic grain growth* is a type of abnormal grain growth in which the abnormal grains grow in an elongated manner, commonly with faceted, straight sides. In porous ceramics, abnormal grain growth is accompanied by breakaway of the boundaries from the pores and, as outlined earlier, must be avoided if high densities are to be achieved.

4.1.3.1 NORMAL GRAIN GROWTH

Normal grain growth in pure, dense, single-phase materials has been analyzed by a number of different approaches [42]. In one of the earliest models, Burke and Turnbull [43] analyzed the diffusion of atoms across an isolated boundary under the driving force of the pressure difference across the curved boundary. *Mean field theories* consider the change in size of an isolated grain embedded in a matrix that represent the average effect of the while array of grains [44–47]. As discussed by Smith [48, 49] during grain growth in real systems, certain topological requirements of a space-filling array of grains must be balanced with the requirements of interfacial tension. These topological requirements are ignored in the model of Burke and Turnbull and in the mean field theories but are considered in the model of Rhines and Craig [50]. More recently, the use of computer simulations has provided a valuable technique for the analysis of grain growth. The simulations of Srolovitz *et al.* [51, 52], employing a Monte Carlo method that allows topological requirements to be taken into account, show a remarkable ability to provide realistic pictures of grain growth and to provide a good fit to some experimental data (Fig. 4.1.8).

The grain growth models predict a kinetic equation of the form

$$G^m = G_0^m + Kt \tag{15}$$

where G is the grain size at time t, G_0 is the grain size at $t = 0$, and K is a temperature-dependent rate constant obeying the Arrhenius equation. For the Burke and Turnbull model and for the mean field theories, $m = 2$ (i.e. parabolic growth kinetics) while the topological model of Rhines and Craig predicts $m = 3$. A non-integral value of $m = 2.44$ has been obtained in the computer simulation depicted in Figure 4.1.8. In practice, grain growth data for dense ceramics yield m values ranging from 2 to 4.

In the model of Burke and Turnbull, the rate constant K for a pure, pore-free material is related to the *intrinsic* mobility of the boundary, M_b, by [2]

$$K = 2\alpha M_b \gamma_{gb} \tag{16}$$

where α is a numerical constant that depends on the shape of the grains and γ_{gb} is the grain boundary energy. The mobility is related to the diffusion coefficient for the atoms across the boundary, D_a, by

$$M_b = \frac{D_a}{kT}\left(\frac{\Omega}{\delta_{gb}}\right) \tag{17}$$

where k is the Boltzmann constant, T is the absolute temperature, Ω is the atomic volume, and δ_{gb} is the grain boundary thickness.

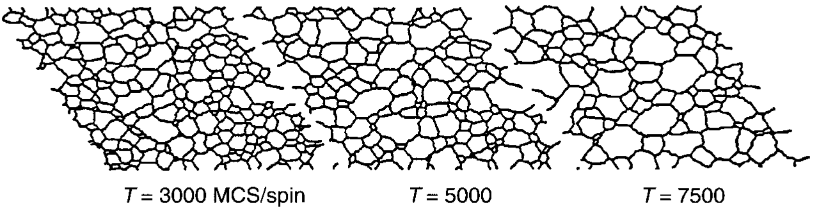

FIGURE 4.1.8 Grain growth in a dense polycrystalline solid determined by computer simulation employing a Monte Carlo method (from Ref. [51], with kind permission of Elsevier, Oxford).

The grain growth models based on the evolution of a single, identified grain do not consider the evolution of the *distribution* of grain sizes with time. As a first approximation, the grain growth rate depends on the difference between the grain size at the mode and at the mean of the distribution. Practically, this means that the rate of grain growth will be higher for a highly skewed distribution (i.e. a distribution with a wide distribution of grain sizes in which the mean grain size is significantly greater than the mode). The rate of grain growth should also be zero for a symmetrical distribution, although it would become broader and shallower with time. A monosize or narrow initial distribution, as may be produced from particles with the same size, will first broaden without an increase in the average grain size. After some incubation time, grain growth takes off, with the average grain size increasing with time.

4.1.3.2 ABNORMAL GRAIN GROWTH

Microstructures of polycrystalline ceramics that have been heated for some time at a sufficiently high temperature often show very large (abnormal) grains in a matrix of finer grains (Fig. 4.1.9). It is important to understand and to be able to control abnormal grain growth for two main reasons [53]. First, the occurrence of abnormal grain growth during sintering limits the attainment of high density. For example, the pores trapped in the abnormal grain shown in Figure 4.1.9 are difficult to remove. Second, the large abnormal grains are commonly detrimental to the properties of the material. An important goal in practical sintering is therefore the suppression of abnormal grain growth. As described later, this is commonly achieved through the use of dopants.

Considerable effort has been devoted to the experimental and theoretical study of abnormal grain growth in ceramics [45, 54–57]. While some insight into the problem has been achieved, the process is not well understood. Earlier explanations considered that the grain size distribution of the starting material was the major factor leading to abnormal grain growth. They were based on the Hillert theory of grain growth [45], which predicted that any grain with a size greater than twice the average grain size would be predisposed to growing abnormally. This explanation is not supported by recent computer simulations [58] and theoretical analysis [59], which show that although the large grains grow, they do not outstrip the normal grains. The normal grains grow at a faster relative rate so that the large (abnormal) grains eventually return to the normal size distribution. The size effect is therefore not a sufficient criterion for abnormal grain growth. Inhomogeneities in chemical composition, liquid phases, and particle packing have long been suggested as possible causes of abnormal grain growth.

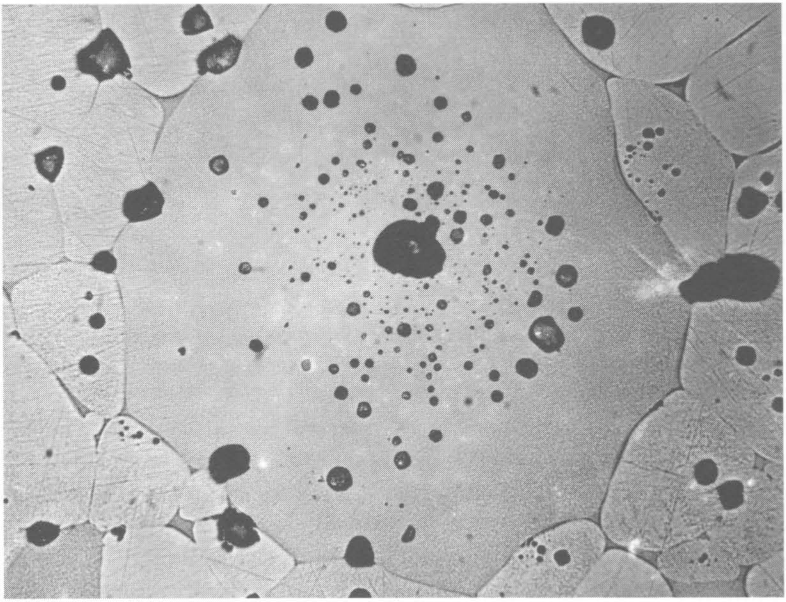

FIGURE 4.1.9 Abnormal grain growth in an MgO ceramic. The pores trapped inside the abnormal grain are difficult to remove, thereby leading to residual porosity in the sintered material (magnification = 700).

Computer simulations and theoretical analysis indicate that true, abnormally rapid grain growth can occur if the boundary of the abnormal grain has a higher mobility or a lower energy than the surrounding matrix grains [60–62]. Grain orientation and grain boundary structure are two factors that can lead to variations in the mobility and energy of grain boundaries. Boundaries of large abnormal grains often show faceting on low-index crystallographic orientations. Frequently, the growth planes are those with low surface energy. Low-energy boundaries often have a lower mobility. Growth that is slow normal to and rapid parallel to the low-energy surfaces often lead to plate-like abnormal grains.

Abnormal (anisotropic) grain growth in Al_2O_3 has received considerable attention, largely based on attempts to understand the role of MgO in suppressing abnormal grain growth in this system [63]. While the single most important role of MgO is the reduction of the boundary mobility [64], it is also recognized that MgO plays an important role in reducing the anisotropies in the surface and grain boundary energies and in the boundary mobilities [65–67]. Doping of Al_2O_3 with TiO_2 has been observed to enhance the formation of elongated, faceted grains [68, 69].

While the suppression of abnormal grain growth forms a key goal in sintering, the ability to exploit abnormal grain growth in a *controlled* manner can

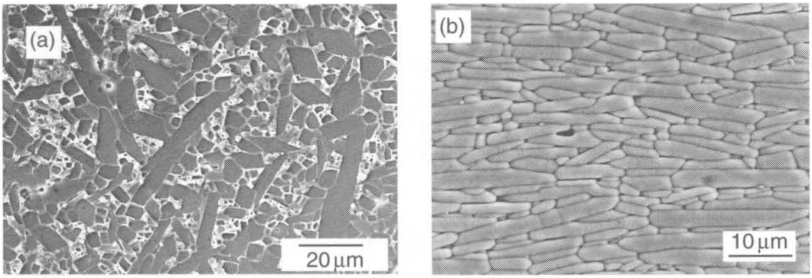

FIGURE 4.1.10 Exploitation of abnormal (anisotropic) grain growth for the production of (a) self-reinforced mullite with enhanced fracture toughness and (b) bismuth titanate ceramic with anisotropic dielectric properties.

provide significant property advantages in several ceramic systems. The growth of a controlled distribution of elongated (abnormal) grains in a matrix of finer grains (Fig. 4.1.10a) has been employed to produce a significant enhancement of the fracture toughness of silicon nitride [70], silicon carbide [71], and mullite [72]. Alignment of the abnormally growing grains (Fig. 4.1.10b) by the process of templated grain growth [73], hot-pressing, or sinter forging has been used to achieve anisotropic dielectric properties in layered-structured ferroelectrics such as bismuth titanate [74, 75]. Abnormal grain growth has been used effectively for many years to produce some single-crystal ferrites by seeding a fine-grained material with a large single crystal. The method has been used more recently to grow barium titanate [76] and lead-magnesium niobate [77] single crystals from polycrystalline materials.

4.1.3.3 OSTWALD RIPENING

The basic theory of Ostwald ripening was developed by Greenwood [78], Lifshitz and Slyozov [79], and Wagner [80], and is generally referred to as the LSW theory. The theory applies strictly to a dilute dispersion of particles in a solid, liquid, or gaseous medium. The characteristic feature of coarsening is that at any given time, particles smaller than a critical size will dissolve, surrounding themselves with a zone of excess solute that will find its way to particles larger than the critical size. The rate-limiting step can be either diffusion between the particles or the deposition or dissolution of atoms at the particle surfaces (reaction controlled growth). In either case, the theory predicts that at some later time, a *self-similar* (steady-state) particle size distribution is approached asymptotically in which the growth of the critical radius, r^*, follows a simple law of the form given earlier by Eq. 15 for normal grain

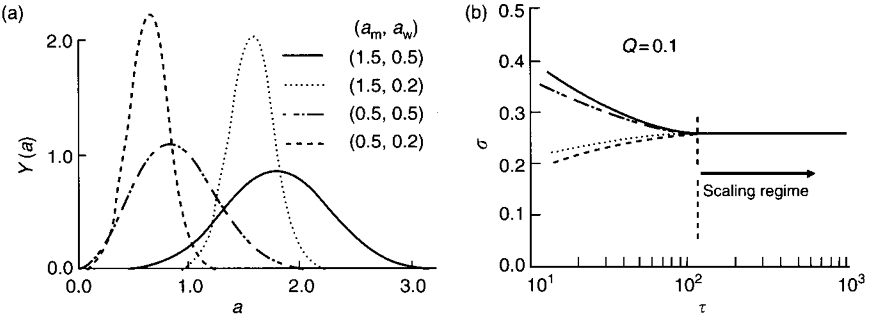

FIGURE 4.1.11 Effect of initial particle size distribution (a) on the time variation of the standard deviations of the distribution and the rate-coarsening rate (b) (after Ref. [84], with kind permission of Elsevier, Oxford).

growth:

$$(r^*)^m = (r_0^*)^m + Kt \tag{18}$$

where K is a temperature-dependent rate constant, t is the time, and m is an exponent that depends on the rate-controlling mechanism: $m = 3$ for diffusion control and $m = 2$ for surface reaction control.

The LSW theory has been the subject of considerable study and revision [81]. A key factor is the interaction between the particles when the dispersion of particles in the medium is no longer dilute. Ardell [82] found that for diffusion control, the exponent $m = 3$ is still valid but the self-similar size distribution approaches that for reaction control (i.e. it is broader and more symmetrical) when the volume fraction of particles is greater than ~0.2. Another important factor is the approach to the steady-state LSW distribution. As shown in Figure 4.1.11, for a modified Gaussian distribution of initial particle sizes with varying maximum value, a_m, and width, a_w, an analysis by Enomoto *et al.* [83, 84] indicate that for distributions with a broad width, the standard deviation of the distribution function decreases to the characteristic time-invariant value, while for systems with a narrow width, the standard deviation increases to the time-invariant value. This behavior during the transient regime indicates that the self-similar state acts as a strong attraction for the evolution of the particle size distribution.

4.1.3.4 CONTROL OF GRAIN GROWTH

The most effective approach for inhibiting grain growth involves the use of additives (*dopants*) that are incorporated into the powder to form a solid solution [14, 15, 53]. The concentration of the dopant (the *solute*) is often believed to

TABLE 4.1.2 Examples of Dopants Used for Grain Growth Control in Some Common Ceramics

Host	Dopant	Concentration (at %)	Reference
Al_2O_3	MgO	0.025	[63, 93]
$BaTiO_3$	Nb; Co	0.5–1.0	[94, 95]
ZnO	Al	0.02	[96]
CeO_2	Y; Nd; Ca	3–5	[91, 92]
Y_2O_3	Th	5–10	[97]
SiC	(B + C)	0.3B + 0.5C	[98]

be well below its solid solubility limit in the ceramic (the *host*) but this is not clear in some systems. Examples of systems where the dopant approach has been used successfully are given in Table 4.1.2. The effectiveness of the dopant in suppressing grain growth is often found to depend on its ability to segregate at the grain boundaries. Segregation may occur right at the disordered "core" of the grain boundary or in an adjacent space-charge layer [85–89].

The inhibition of grain growth is believed to occur by a mechanism of *solute drag*. In this mechanism, a strong interaction occurs between the segregated solute and the grain boundary so that the solute must be carried along with the moving boundary. Solute diffusion across the boundary is assumed to be slower than that of the host atoms and therefore becomes rate controlling. In the solute drag theory put forward by Cahn [90], the boundary mobility of the doped material is given by

$$M_b' = \frac{D_b \Omega}{4kT\delta_{gb} Q C_0} \tag{19}$$

where D_b is the diffusion coefficient for the solute atoms across the boundary of width δ_{gb}, Ω is the atomic volume of the host atoms, k is the Boltzmann constant, T is the absolute temperature, Q is a partition coefficient for the solute distribution between the boundary and the lattice, and C_0 is the concentration of the solute atoms in the lattice. According to Eq. 19, the boundary mobility is directly proportional to the diffusivity of the solute across the boundary and inversely proportional to the segregated concentration of the solute (QC_0). This indicates that aliovalent solutes with larger ionic radii than the host would be effective for suppressing grain growth. While the influence of trivalent cations on the grain growth of CeO_2 may be consistent with this prediction [91, 92], in general the choice of an effective dopant is complicated because of the multiplicity of the dopant role.

At low driving force or low boundary velocity [99], the mobility of the boundary is limited by solute drag and is given by Eq. 19. With increasing velocity, the boundary breaks away from the solute and has a mobility given by the intrinsic value (Eq. 17). Observations indicate that the boundary motion is not uniform but that it starts and stops as if making transitions between the solute-drag and intrinsic regimes or between different solute drag regimes [100].

Another effective approach for grain growth control, but one that is less widely used, involves the use of fine, inert, precipitates at the grain boundaries. An example is the use of ZrO_2 particles to control the grain growth of Al_2O_3 [101]. The precipitates inhibit grain growth by a pinning mechanism suggested by Zener in a communication to Smith [48]. According to Zener, the matrix reaches a limiting grain size given by

$$G_{\max} = \frac{2\alpha r}{3f} \tag{20}$$

where α is a geometrical constant that depends on the shape of the matrix grains, r is the radius of the precipitates (assumed to be spherical), and f is the volume fraction of the precipitates. Recent work by Stearns and Harmer [102, 103] indicates that the pinning particles are not distributed as randomly as the Zener model assumes. By incorporating the observed fraction of pinning particles at the grain boundaries into the Zener model, a modified relationship was developed to describe the grain growth data of Al_2O_3 containing fine SiC particles.

4.1.3.5 GRAIN GROWTH AND PORE EVOLUTION IN POROUS COMPACTS

In porous powder compacts, grain growth is very limited in the initial stage of sintering but coarsening of the microstructure can occur by surface diffusion and vapor transport. The mechanism most commonly cited for coarsening in this early stage of sintering is that suggested by Greskovitch and Lay [104]. It assumes that the coarsening processes (surface diffusion; vapor transport) lead to rounding of the particle shapes and growth of the necks between the particles, thereby producing the structural changes for boundary migration to be energetically favorable. The grain growth rate increases in the intermediate stage and migration of the boundaries leads to coalescence of the pores so that the average size of the pores also increases. Grain growth is most pronounced in the final stage when the pores pinch off and become isolated. Normal grain growth has been analyzed using an idealized model consisting of a nearly spherical pore on an isolated grain boundary. The kinetics of normal grain growth can be described by Eq. 15 where value of the exponent m (2–4) now depends on mechanism of the pore motion and the extent of the drag produced by the pores on the boundaries [53]. Several mechanisms have the same value of m so that an unambiguous determination of the grain growth mechanism from experimental data is difficult.

An understanding of pore evolution during sintering is important for a broader understanding of the microstructural evolution. However, very few investigations have been devoted to pore evolution due largely to the difficulty of quantitative analysis and the time-consuming nature of detailed stereological characterization. On the basis of stereological observations, Rhines and DeHoff [105] showed that the pore network changes by collapse of the network and the reforming of a new network with lower connectivity. The variation of the open and closed porosity during the sintering of a heterogeneously packed UO_2 powder was studied by Coleman and Beeré [106]. The results showed that the volume of closed porosity started to increase when the open porosity had decreased to 15 vol%. For a homogeneously packed powder, it may be expected that the formation of closed porosity would occur more suddenly and when the volume of open porosity had decreased to a value of less than 10%.

4.1.3.6 INTERACTIONS BETWEEN PORES AND GRAIN BOUNDARIES

The attainment of high density during sintering, as outlined earlier, depends on the ability to stabilize the microstructure such that the pores and the grain boundaries remain attached. For an idealized geometry of an isolated, spherical pore at a grain boundary, typical of an idealized microstructure in the final stage of sintering, the interaction between the pore and the boundary has been used to determine the conditions for pore attachment and breakaway. A migrating boundary will apply a force on any pore situated at the boundary and will try to drag it along [107, 108]. As illustrated in Figure 4.1.12, the force causes the pore to change its shape. The leading surface of the pore becomes less strongly curved than the trailing surface. The difference in curvature causes a flux of matter from the leading surface to the trailing surface. The result is that the pore attempts to move with the boundary.

For each of the mechanisms indicated in Figure 4.1.12, analysis of the atomic flux from the leading surface of the pore to the trailing surface yields a pore mobility, M_p, of the form [53]:

$$M_p = \frac{AD\Omega}{kTr^n} \tag{21}$$

where A is a constant, Ω is the atomic volume, k is the Boltzmann constant, T is the absolute temperature, r is the radius of the pore, D is the appropriate

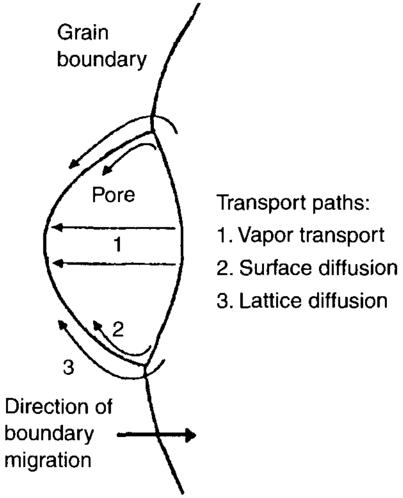

FIGURE 4.1.12 Possible transport paths for a pore moving with a grain boundary.

diffusion coefficient, and m is an exponent that depends on the mechanism: $D = D_s$ and $m = 4$ for surface diffusion; $D = D_l$ and $m = 3$ for lattice diffusion; $D = D_g$ and $m = 3$ for vapor transport. According to Eq. 21, fine pores are highly mobile and are better able to remain attached to the boundary. In practice, strategies for avoiding breakaway of the boundary (abnormal grain growth) are based mainly on suppressing grain growth (reducing M_b) through the use of dopants.

4.1.3.7 MICROSTRUCTURAL MAPS

Brook [109] developed a method to visualize the interaction between the pore and the boundary during sintering. Two situations can be visualized: (i) the pore remains attached to the migrating boundary (referred to as *attachment*) or (ii) the boundary breaks away, leaving the pore behind (*separation*). The conditions under which each situation becomes important are determined as functions of the grain size and the pore size. The results are represented on a diagram, commonly referred to as a *microstructural map*, of the grain size versus the pore size (Fig. 4.1.13). With the pores attached to the boundary, the mobility of the boundary can be controlled by pore drag (*pore control*) or by the intrinsic boundary parameters (*boundary control*). Pore–boundary separation is predicted to occur only for certain ratios of grain to pore size. Brook also considered

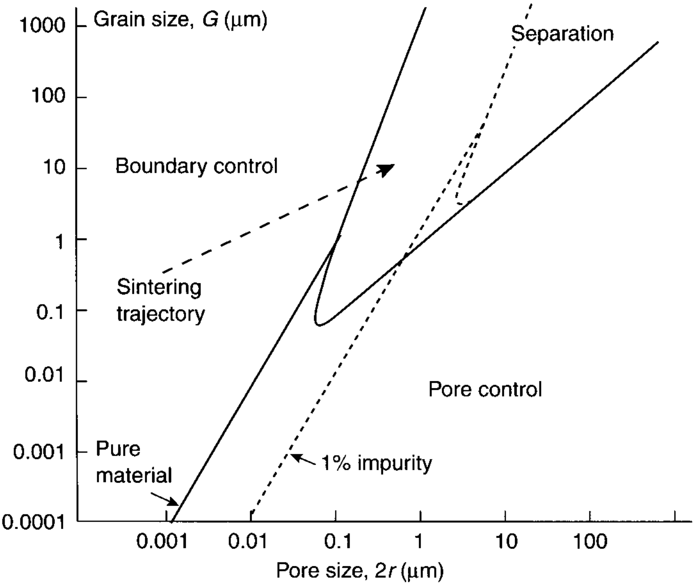

FIGURE 4.1.13 Grain size versus pore size map showing the conditions for pore attachment and pore separation. A trajectory for densification accompanied by coarsening of the microstructure is shown. If the separation region is not intersected, then the attainment of complete densification is possible (from Ref. [109], with kind permission of Elsevier, Oxford).

the effect of a segregated impurity (solute) on the boundary mobility. The mobility limited by solute drag is lower than the intrinsic mobility, allowing larger pores to migrate with the boundary before separation. The separation region is therefore shifted to larger grain and pore sizes. In the sintering of ceramics where the densification is accompanied by coarsening, both the average grain size and the average pore size increase, as shown by the trajectory on Figure 4.1.13.

A modification of the grain size versus pore size map was used by Berry and Harmer [110] to show the sintering trajectories for Al_2O_3 on a *grain size* versus *density* map (Fig. 4.1.14). The influence of dopants and other variables can now be discussed in terms of their effects on the separation region and the sintering trajectory. For the achievement of high density during sintering, the separation region must be avoided. According to Figures 4.1.13 and 4.1.14, the use of a dopant that reduces the boundary mobility has the effect of shifting the separation region to higher grain sizes, thereby making it easier for the trajectory to bypass the separation region. Flattening of the grain size versus density trajectory by enhancing the ratio of the densification rate to the grain growth rate is also effective. This can be achieved by the use of a dopant that lowers the boundary mobility or by selecting a heating schedule that enhances the densifying mechanisms relative to the coarsening mechanisms (see Section 7).

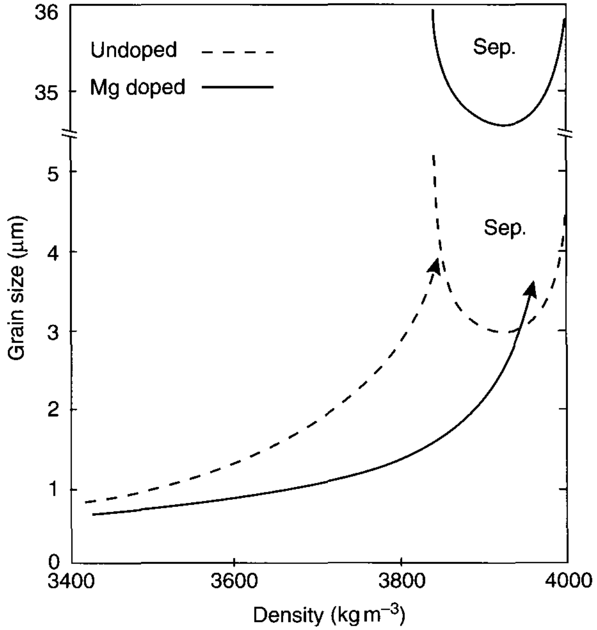

FIGURE 4.1.14 Grain size versus density map for undoped Al_2O_3 and for Al_2O_3 doped with 250 ppm MgO. The depicted trajectory for the doped Al_2O_3 is the result of raising the surface diffusivity by a factor of 4, reducing the lattice diffusion coefficient by a factor of 2, and reducing the grain boundary mobility by a factor of 34 (courtesy of M. P. Harmer).

While the microstructural maps provide a valuable method for representing the interaction between densification and coarsening, the idealized geometry of the assumed microstructure (a spherical pore on an isolated boundary of uniform curvature) means that the maps have limited applicability to actual final-stage microstructure. Furthermore, factors such as grain size distribution, pore size distribution, number of pores, and the dihedral angle will affect the simple relationships between pore size and boundary curvature assumed for separation [108, 111, 112].

4.1.4 LIQUID-PHASE SINTERING

In many sintering processes, the intervention of a liquid phase is commonly sought to assist in the densification. The purpose is usually to enhance densification rates, achieve accelerated grain growth, or to produce specific grain boundary properties. In these materials, the distribution of the liquid and of the

TABLE 4.1.3 Some Liquid-Phase Sintering Systems

System	Reference
Alumina + $Mg_3Si_4O_{10}(OH)_2$ (talc)	[113]
$ZnO + Bi_2O_3$	[114]
$SiC + Y_2O_3 + Al_2O_3$	[115]
Si_3N_4 + MgO, Sialons	[116, 117]
$BaTiO_3 + B_2O_3$	[118]

resulting heterophases after densification is of critical importance to the properties of the sintered body. Typically, the amount of liquid involved is small, a few volume percent, which can make precise control over the composition of the liquid difficult. Examples of theses are silicon ceramics, such as SiC and Si_3N_4, where the native silicon oxide film on the starting powders is only known approximately, while the silica participates in forming the liquid phase together with the intentionally introduced additives. In some instances, such as the densification of alumina, the amount of liquid phase is quite small, and so difficult to detect that numerous studies that were believed to be solid-state sintering actually involved liquid silicate phases. The solidified liquid phase could only be revealed by careful high-resolution transmission electron microscopy. Some examples of common liquid-phase sintering systems are listed in Table 4.1.3.

A related process is *activated sintering*. In this case, minor amounts of additives that segregate strongly to the grain boundaries can enhance grain boundary transport rates significantly, accelerating densification even below any eutectic temperatures in the additive/host system. Examples are found in the sintering of ZnO with Bi_2O_3 additive [119], and Al_2O_3 with CaO [120]. However, in many other cases there is no clear difference in the principles involved in activated sintering [121] and in liquid-phase sintering, other than the activated system involving the addition of less than 1% additive for which the resulting liquid grain boundary film can be difficult to detect. Clearly, the enhanced densification rates achieved by liquid-forming additives are only of interest if the properties of the material remain within useful bounds. For example, liquid-forming additives tend to degrade high-temperature properties such as creep and fatigue resistance, because of persistent intergranular films of nanometer thickness. An example of such a film is shown in Figure 4.1.15.

Liquid-phase sintering is generally regarded as proceeding in a sequence of dominant stages: (a) melting of the liquid-forming additive and redistribution of the liquid; (b) rearrangement of the majority solid phases driven by capillary stress gradients; (c) densification and shape accommodation of the solid phase involving solution-precipitation; (d) final densification driven by residual porosity in the liquid phase (Fig. 4.1.16).

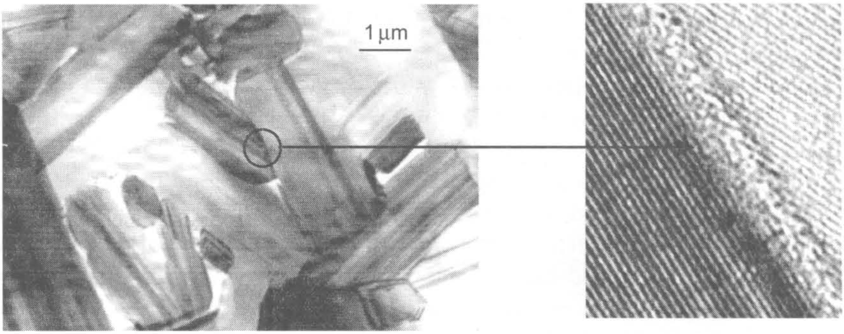

FIGURE 4.1.15 Persistent amorphous grain boundary phase, approximately 1-nm thick, in SiC containing Al, B and C as sintering additives (from Ref. [122]).

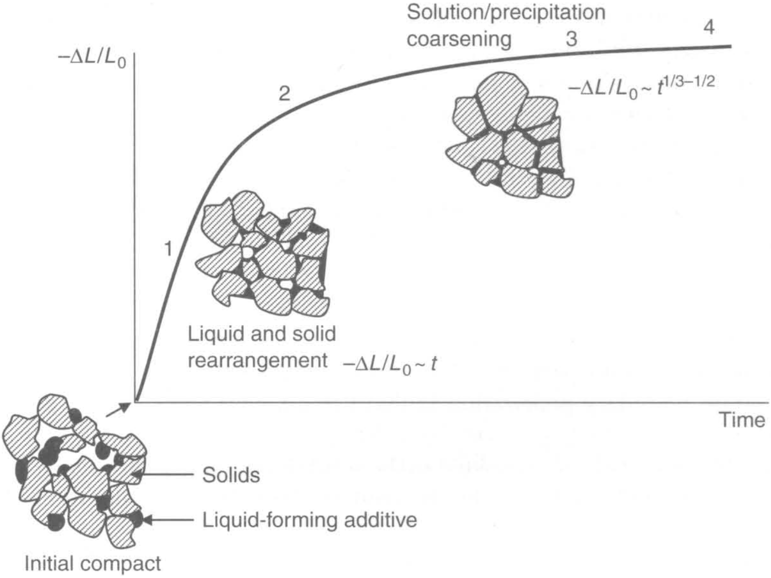

FIGURE 4.1.16 Schematic evolution of powder compact during liquid-phase sintering. The various stages are overlapping significantly.

4.1.4.1 LIQUID-PHASE REDISTRIBUTION

Capillary stress gradients can be significant when submicron liquid-phase surface curvatures are present. For a surface energy of about 1 J/m^2 and a radius of curvature of 0.5 μm, pressure differentials within the sample can reach several MPa, sufficient to cause rapid fluid flow and particle rearrangement when the compact's effective viscosity is still relatively low. The pressure gradients will cause fluid to flow from regions with large liquid pores to regions of smaller liquid pores, and as a consequence from the surface to the interior of the compact. This principle leads to a sequential pore filling [123]. However, in the final stages of sintering continued densification of the solid particle skeletal network can eventually lead to partial expulsion of the liquid phase. One difficulty in modeling liquid redistribution is that local liquid surface curvature depends sensitively on local geometry, so quantitative statements can only be made for highly idealized microstructures [124]. Although these are highly idealized rigid particle arrays, such models can provide further insight in the process of liquid redistribution.

Rearrangement is typically fast, but kinetics are only of interest to the extent that, together with grain growth, they are an integral part of microstructure development. Once the rearrangement stage is over, models that do not incorporate simultaneous grain growth lead to shrinkage rates proportional to time$^{1/3}$ when diffusion through the liquid is rate controlling or time$^{1/2}$ when liquid/solid phase boundary reactions are rate controlling. These models further assume that the grain boundary liquid phase does not change composition or structure. This is not always the case. There are now several examples where the composition of the grain boundary film is found to be different from that of the liquid in the adjacent triple junction or even from boundary to boundary [125, 126], as shown in Figure 4.1.17. It is quite likely that such is more the rule than the exception.

A second-stage rearrangement has also been recognized. This refers to the instance in which the liquid phase is thought to penetrate the grain boundaries of dense, multigrain particles. A minimum requirement for partial or complete grain boundary penetration is that the dihedral angle is near zero (see Figure 4.1.18).

The dihedral angle, ψ, is related to the solid/liquid interfacial energy, γ_{sl} and the grain boundary energy γ_{gb} by the vector force balance, similar to Eq. 5:

$$2\gamma_{sl}\cos(\psi/2) = \gamma_{gb} \tag{22}$$

In the event that sufficient liquid is present and interfacial energies are fairly uniform, this may lead to a microstructure in which individual, rounded grains are dispersed in the liquid. Such a microstructure is commonly seen in metallic systems, as shown in Figure 4.1.19, and in some ceramic systems such as MgO/silicate [127]. In many ceramic systems, angular or ideomorphic grain shapes are more commonly found as a result of liquid-phase sintering.

While liquid redistribution is relatively easy, it is remains desirable to start with a compact that is as homogeneous as practical, for example, by using powders in which the particles are pre-coated with the liquid-forming phase: the

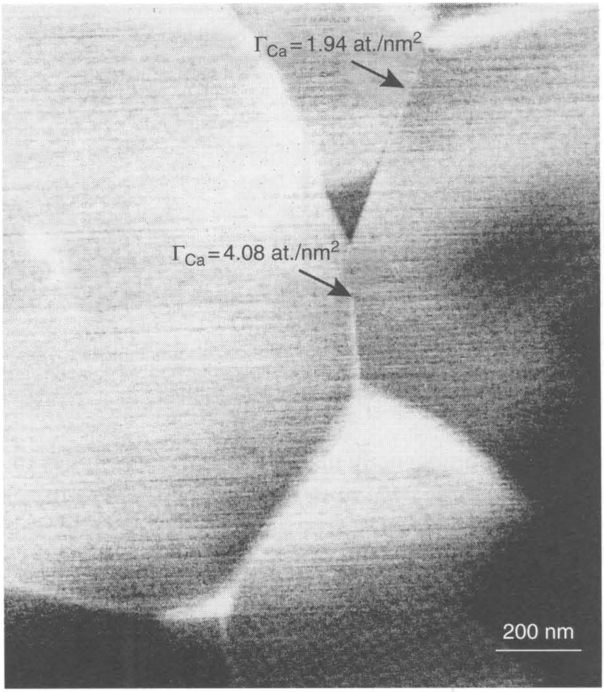

FIGURE 4.1.17 STEM image showing two neighboring grain boundary films with remarkably different calcium excess in calcia-doped silicon nitride (from Ref. [125]).

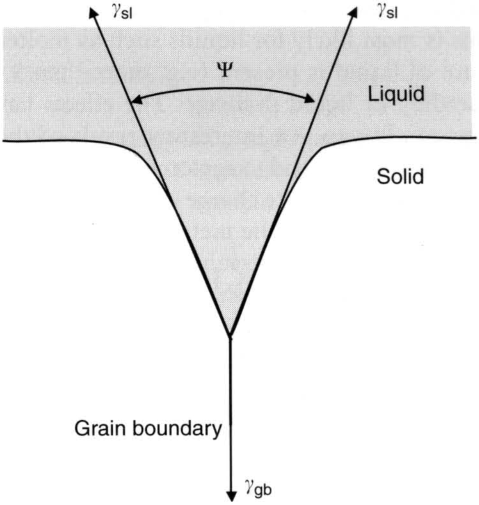

FIGURE 4.1.18 Dihedral angle for liquid at a grain boundary.

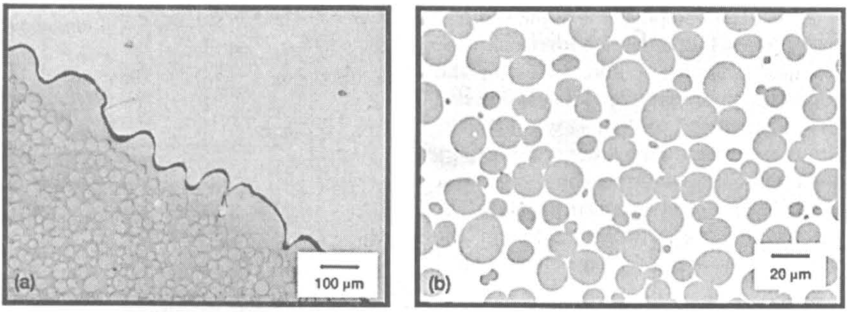

FIGURE 4.1.19 Micrographs of 78W–15.4Ni–6.6Fe after liquid-phase sintering for 1 min in microgravity at 1507°C: (a) low magnification view of sample edge and wavy solidified liquid; (b) high magnification view of sample interior showing solid grain agglomeration (courtesy R. M. German).

same concerns about homogeneity of starting compact applies to liquid-phase sintering as it does to solid-state sintering. Methods whereby powders can be coated include fluidized bed vapor deposition, and chemical precipitation from aqueous suspensions [128].

4.1.4.2 EFFECTS OF GRAVITY

The relatively low effective viscosity of powder compacts containing a liquid phase leads to ready creep, and the weight of the sample itself can cause significant deformation. Judicious support for large pieces is thus necessary, and has been longtime practice [129]. Additional problems are the possibility of liquid redistribution. This is most likely for liquids such as molten metals, or when a significant amount of liquid is present (e.g. more than 5 vol%) resulting in possible particle settling or liquid drainage. The effects have been examined under microgravity conditions. An interesting result of these studies is that solids suspended in a liquid still tend to agglomerate, as shown in Figure 4.1.19. Since this is a metallic system, surface charge effects, as in colloidal suspensions, cannot be active. It is possible that the metal particles are propelled, colliding and joining, as a result of uneven dissolution/precipitation rates along their surfaces. It is possible that liquid films that may be detected by high-resolution transmission electron microscopy remain at the contact areas.

4.1.4.3 GRAIN BOUNDARY FILMS

Initially, when there is a significant amount of liquid between the grains, the thickness of the grain boundary is kinetically determined. The thinning rate,

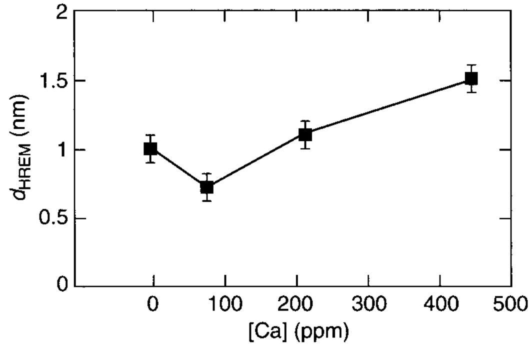

FIGURE 4.1.20 Equilibrium grain boundary thickness measured by HREM (d_{HREM}) plotted against bulk calcium doping level in silicon nitride (from Ref. [133]).

a consequence of capillary viscous flow, of the liquid film at a grain boundary of fixed cross-section has been calculated by Lange [130] as proportional to d^5, where d is the instantaneous film thickness. This predicts an infinite time for the film thickness to reach zero. However, when the film gets very thin, that is, in the nanometer range, effects other than viscous flow become dominant, including charge interactions between surfaces [131], as well as structural and chemical forces [132]. Compositional effects on what appears to be an equilibrium grain boundary film thickness have been the subject of careful investigation. Some of the results are shown in Figure 4.1.20.

4.1.4.4 EFFECTIVE STRESS

Concepts that have been developed in soil mechanics [134, 135] can also be applied to liquid-phase sintering. Considering a cross-section that runs through the particle–particle contacts, the particle network, or skeleton, will carry an effective stress given by

$$\sigma_y^{\text{eff}} = \left(\sum F_{iy}\right)/a \qquad (23)$$

where F_{iy} is the component of the force in the y direction at the ith particle–particle contact, and a is the external cross-section of the sample. In the absence of any externally applied stress and pressure gradients, the effective stress is then

$$\sigma_y^{\text{eff}} = p(1 - a) \qquad (24)$$

where p is the capillary pressure in the liquid phase.

When a significant amount of liquid is present between the particles, the effective stress will be less than the equilibrium one, because the effective stress causes liquid to flow out of the contact areas. Once the liquid films become very thin, kinetic or other factors [136] obstruct fluid flow, and the effective stress will approach the equilibrium one. This effective stress is the driving force for solution precipitation mechanisms, together with Ostwald ripening processes. The effective stress concept is similar to the sintering stress multiplied by the stress concentration factor discussed earlier.

The capillary pressure, p, follows from the surface curvature of the liquid phase, which is determined by the particle size, the solids volume, and the liquid volume. In simple, idealized geometries the equilibrium curvature can be readily computed from geometrical considerations. Additionally, computational programs are now available to calculate such curvatures for a number of more complex geometries. In practice, the capillary pressure is not readily determined because of the distribution of particle sizes, complex packing geometries, and distribution of pore sizes.

In the first stage of consolidation, densification is rapid due to rearrangement of the particle skeleton, rapid dissolution of small network particles, and removal of liquid between network particles. Rearrangement of the initial particle network may occur in as little as a few minutes. Computational approaches to rearrangement have recently been made [137]. Once a quasi-steady-state grain boundary film is established, densification proceeds similar to solid-state densification at a comparatively enhanced rate. Rapid transport in the liquid phase makes grain growth more prominent in liquid-phase sintering. Inclusion of a dispersion of inert particles can assist in limiting grain growth.

4.1.4.5 ROLE OF THE WETTING ANGLE

The wetting angle, θ, for the liquid/solid/vapor system depends on the various interfacial energies, and is usually referred to a droplet of liquid on a flat solid surface. While this does not represent the full equilibrium, it is often cited as such, and is given by

$$\cos\theta = (\gamma_{sv} - \gamma_{sl})/\gamma_{lv} \tag{25}$$

where γ_{sv}, γ_{sl}, and γ_{lv} are the specific energies of the solid/vapor, solid/liquid, and liquid/vapor interfaces, respectively. No correction for surface curvature is considered, although the surface will support a curvature-dependent stress. The corrections are generally considered negligible. The γ_{lv} values of many inorganic melts, such as silicates, are often between 0.1 and 0.5 J/m^2, with 300 mJ/m^2 cited as a most common value for molten silicates [138], with surface tension for liquids, liquid metals, and metal oxides ranging as high as 2 J/m^2. The change of surface tension with temperature for melts such as silicates has been less well established. There are some indications in the older literature that the surface tension of a number of glasses would increase at lower temperatures [138, p. 208], and this might account for phenomena such as dewetting at lower temperatures. Compositional changes also modify the surface tension; as an example, the surface tension of Fe_xO–SiO_2 melts round 1300°C decreasing approximately linearly, from about 550 mJ/m^2 at zero wt% SiO_2 to 350 mJ/m^2 at 45 wt% SiO_2 [139].

The geometries that have been considered so far for model determination of the wetting geometry ignore the complication that for effective liquid-phase sintering, the particles have to be partially soluble in the liquid phase, leading to detailed wetting geometries or liquid distribution that requires modification of the simple two-dimensional Young's equation. These effects, including transient ridge formation near the triple junction, have been examined by Cannon *et al.* [140]. Figure 4.1.21 shows some of the configurational changes when solubility of the solid in the liquid is taken into account.

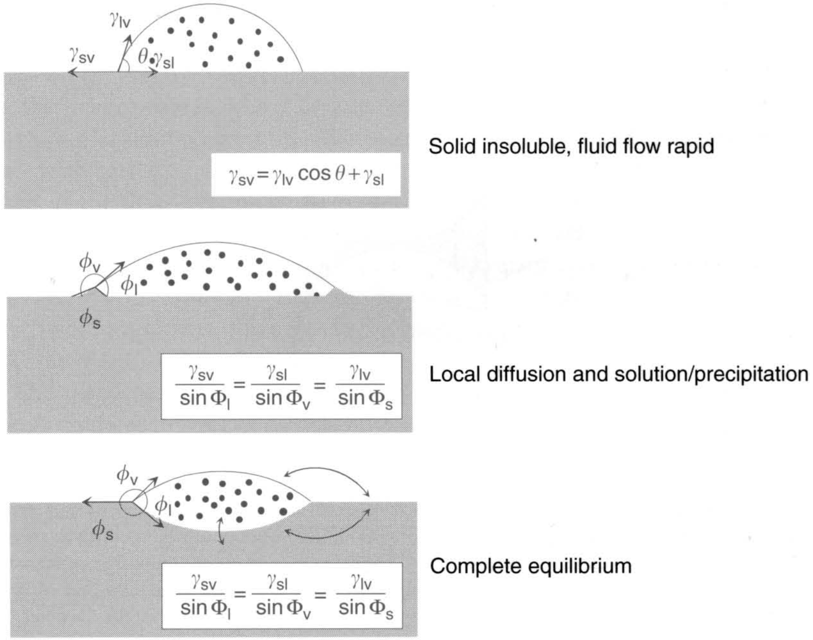

FIGURE 4.1.21 Shape changes associated with partial solubility of the solid in the liquid [140] (courtesy R. M. Cannon).

During fast heat-up and melting, where the rapid densification occurs, it may be difficult to draw a clear distinction between reactive wetting and non-reactive wetting. Reactive wetting can then be taken as referring to the case where the liquid and the solid react to form a new solid phase.

4.1.4.6 RELATIVE AMOUNT OF LIQUID PHASE

The distribution of the liquid phase depends on the dihedral angles and the relative amount of liquid phase, as well as on the porosity. For contact angles larger than zero, it becomes possible to have the liquid phase actually produce repulsive forces rather than attractive forces between the particles. For such a case, further densification can only proceed by grain growth. This is readily appreciated by considering the neutral effect case as a function of liquid volume,[2] as illustrated approximately in Figure 4.1.22. Calculations of capillary forces between unequal particles were discussed by Huang *et al.* [141]. A more detailed example using the *surface evolver* can be found in the article by Carter [142].

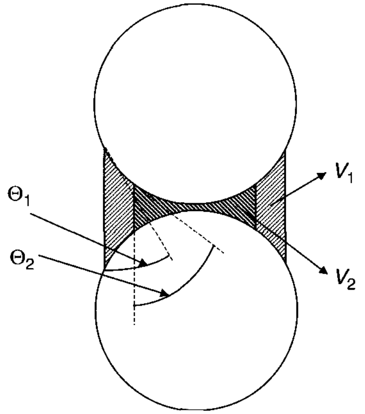

FIGURE 4.1.22 Two-dimensional illustration of the dependence of the neutral volume of liquid phase for a two-particle geometry. At fixed particle separation the neutral conditions will depend on the equilibrium contact angles Θ_i, and the corresponding liquid volumes V_i. With decreasing contact angle, the neutral liquid volume increases. The exact neutral condition in three dimensions still involves some liquid surface curvature when viewed in a two-dimensional section. A liquid volume in excess of the neutral volume produces a repulsive condition between the particles.

---

[2] The actual neutral case still involves some liquid surface curvature in three dimension.

If sufficient liquid is present, initial rearrangement leads to a fully dense material. The relative amount of liquid and solid at this condition depends on the rearranged density of the solids. In the event that the solids could rearrange to approach a dense random packing, then approximately 35 vol% of liquid would fill all the voids space without further solid skeleton densification. Such large volume fractions of liquid are often used in porcelains and in cemented carbides. In the case of clayware and porcelains, the liquid phases are molten silicates that remain as glass after cooling [143]. This gives the ceramic ware glassy appearance, and such ceramics are referred to as vitrified. The precise phase compositions in vitrified ceramics such as triaxial whiteware (clay–feldspar–silica compositions) can, in principle, be determined from the corresponding phase diagrams, although such phase diagrams are often incomplete and difficult to interpret if more than two components need to be considered [144]. In this regard, it is interesting to note that even the "simple" binary system alumina–silica, the subject of numerous investigations, remains a subject of study. One reason is that equilibrium is difficult to determine.

4.1.5 REACTION SINTERING

Reaction (or reactive) sintering is a process whereby new phases are formed during the firing process. Many ceramic systems involve some degree of reaction, for example, silicon ceramics where a small amount of additives are included to react with native oxide. In other systems, second phases are present only during a part of the densification process, and are absorbed in the matrix phase. This is considered transient second-phase sintering, and numerous examples can be found in the literature [145, 146]. Reactive sintering is defined here as the class of synthesis processes in which the major phase results from the reaction of at least two component powders. Some examples of reactive sintering are listed in Table 4.1.4.

The reactions, which are either solid/solid or solid/liquid, typically involve energy changes that are considerably larger than the changes in surface energies,

TABLE 4.1.4 Some Reaction Sintering Systems

Reactant powders	Resulting ceramic	Reference
$3Al_2O_3 + 2ZrSiO_4$	$3Al_2O_3 + ZrO_2$	[147]
$Si_3N_4 + AlN + Al_2O_3$	Sialon	[148]
$SiO_2 + Al_2O_3$	Mullite	[149]
$ZnO + Al_2O_3$	$ZnAl_2O_4$	[150]

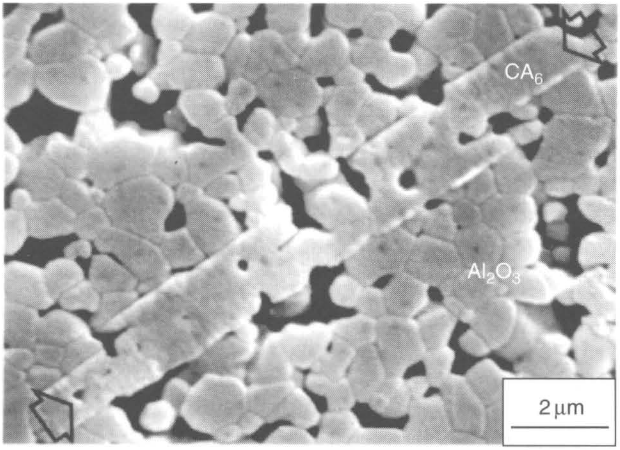

FIGURE 4.1.23 Scanning electron micrograph of calcium hexa-aluminate (CA$_6$ arrowed) formed during the densification of alumina powder mixed with 5 wt% particulate CaO, after 20 h at 1330°C. The plate-shaped CA$_6$ phase replicates the porous alumina matrix during solid-state reaction/grain growth (from Ref. [120]).

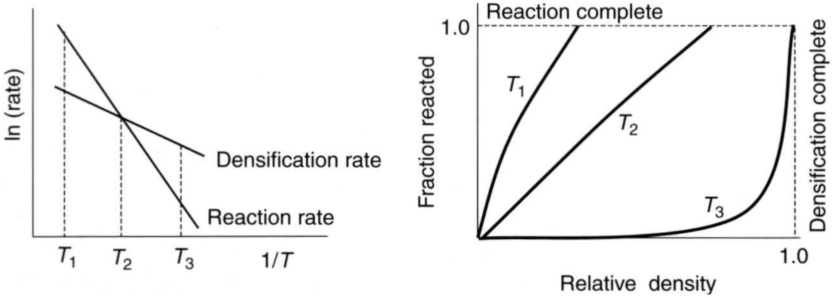

FIGURE 4.1.24 Schematic relationship between densification rate and reaction rate as a function of temperature T, and the resulting process trajectory. If the reaction rate is fast compared to densification, complete reaction can occur with limited densification (after Ref. [147]).

and as a result can lead to microstructures that inhibit densification [120]. An example is shown in Figure 4.1.23.

Qualitatively, it is convenient to consider the reaction and the densification as two separate processes, and put forth a conceptual diagram that illustrates some issues. Such diagrams have been proposed by Yangyun and Brook [147] as shown in Figure 4.1.24. These conceptual arguments lead to the conclusion that the best process is one where densification is completed before reaction can interfere, assuming that there are no deleterious molar volume differences between products and reactants.

An interesting exploitation involving this concept is the reaction sintering of silica-coated alumina and silicon carbide particles. This *transient viscous sintering* process, developed by Sacks *et al.* [151], involves rapid viscous densification due to the persistent presence of the inter-particle silica glass layer, while the subsequent reaction produces dense mullites or mullite–SiC composites.

An example of reaction sintering in which the reaction is delayed until after completion of densification can be found in the work of Claussen *et al.* [152] for the formation of a zirconia–mullite composite from zircon and alumina powders, using a dual-stage processing. In this case, it was possible to achieve nearly full densification at around 1450°C, while the reaction between zircon and alumina only initiated and proceeded to completion at about 1600°C. The resulting ceramic is a nanosize dispersion of monoclinic and tetragonal zirconia in a mullite matrix.

Since energy changes are much larger for chemical reaction than for surface area changes, it would be interesting if reaction energy could be persuaded to drive densification. There is, however, no evidence that the free energy of reaction can act directly as a driving force for densification.

4.1.5.1 INFLUENCE OF PROCESSING PARAMETERS

The temperature T_2, in Figure 4.1.23, where reaction and densification proceed approximately at the same rates, can be affected by the choice of particle sizes, by the transport mechanisms involved in product formation, and by the detailed distribution of the reactant particles. Smaller starting powder sizes, R, accelerate densification with respect to reaction rates, and thus can assist in reaching higher sintered densities. This follows from the general dependence of densification rates on $1/R^m$ (where $m = 3$ or 4) while the reaction rates [153, 154] depend roughly on $1/R^n$ (where $n = 1$ or 2). Apparent activation energies, as implied in Figure 4.1.23, may, however, also be affected by changes in the particle size, so it may not always be possible to achieve full densification prior to reaction simply by reducing the particle sizes of the starting powders.

The importance of the reactant powder distribution and molar volume changes was evident in studies on reactive sintering of $ZnO–Fe_2O_3$ and $ZnO–Al_2O_3$ powders. For $ZnO–Fe_2O_3$, the spinel-phase $ZnFe_2O_4$ forms at nearly constant molar volume, with inter-diffusion of Zn and Fe ions through the spinel product phase. In this case, reaction sintering proceeds without difficulty, as evident in Figure 4.1.25 for well-mixed powders [155].

For $ZnO–Al_2O_3$ a significant molar volume change accompanies the formation of zinc aluminate, and the system is far more sensitive to reactant powder distribution. Significant differences in densification behavior were found for

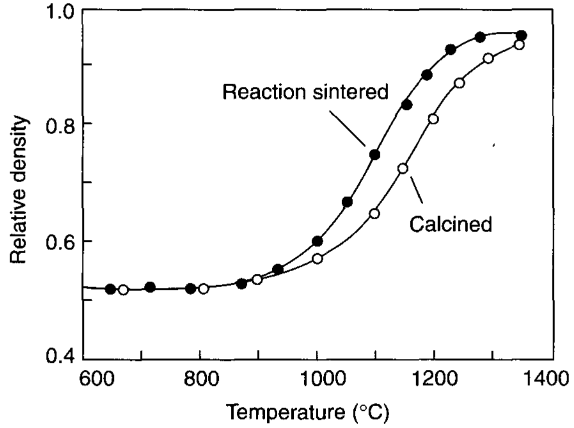

FIGURE 4.1.25 Relative density versus temperature for sintering of ZnO–Fe_2O_3 powder mixtures and for pre-calcined powders of $ZnFe_2O_4$ (from Ref. [155]).

mixed powders compared to ZnO-coated alumina powders prepared by chemical precipitation, as shown in Figure 4.1.26. The expansion produced as a result of the reaction is evident.

4.1.6 CONSTRAINED SINTERING

Densification can be opposed when the sintering matrix has to maintain strain compatibility with a dimensionally invariant phase. Such invariant phases are either dispersions of a second phase or rigid substrates. Variants of these constraints are cases where the second phase has a different densification rate from the matrix. The differential densification rates lead to back stresses in the surrounding densifying matrix that can produce varying degrees of damage. In general, the damage takes the form of higher localized porosity, or more severely, of formation of crack-like defects [157] or film delamination.

4.1.6.1 DISPERSED INERT PHASES

For the case of dispersed inert second phases, an important issue is whether the dispersion forms a continuous skeleton or is agglomerated to some degree. Various models have been proposed to analyze the behavior of well-dispersed systems. In that case, a concentric sphere model is appropriate, in which the

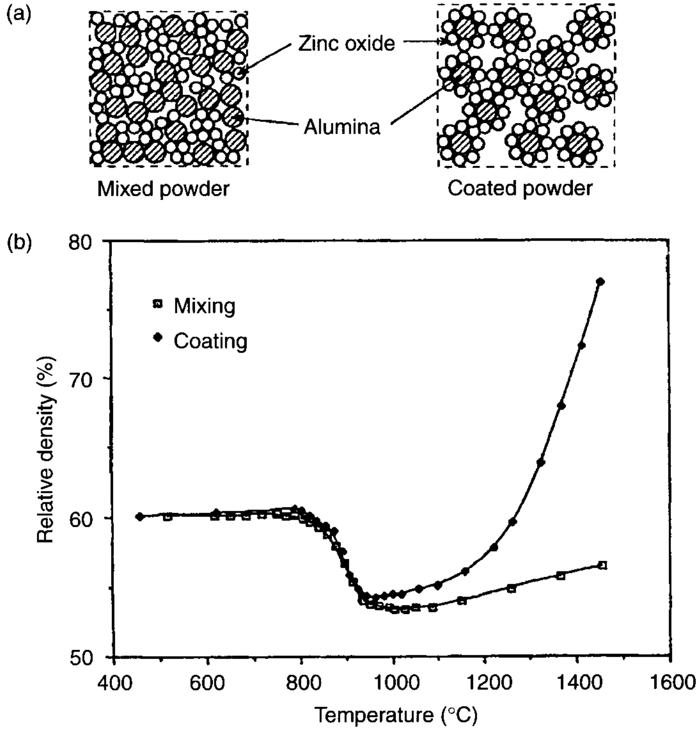

FIGURE 4.1.26 Effect of reactant powder distribution on densification for reaction sintering of ZnO–Al_2O_3. Considerably more densification results for coated powders (from Ref. [156]).

invariant phase is contained as a rigid sphere surrounded by a uniform shell of densifying material. The effects of the back stresses caused by the presence of the rigid particle is then analyzed using a viscoelastic description of the sintering process. However, the system is basically near the viscous limit, predicting relatively small back stresses. Scherer's analysis [158] leads to a linear densification rate of the composite, $\dot{\varepsilon}_c$, that follows from the free (i.e. unconstrained) densification rate of an identical matrix, $\dot{\varepsilon}_{fm}$, predicted by

$$\dot{\varepsilon}_c = [(1-f)K_{cs}/4G_m]\dot{\varepsilon}_{fm} \qquad (26)$$

where f is the volume fraction of the inert inclusions, and K_{cs} is related to the shear viscosity, G_m, and the bulk viscosity, K_m, of the matrix is given by $K_{cs} = 1/(1/4G_m + f/3K_m)$.

Another way of expressing the results is to invoke the densification rate of the composite as predicted by a simple, linear rule of mixture, which for an inert and uniformly dispersed inclusion phase would be

$$\dot{\varepsilon}_{\mathrm{c}}^{\mathrm{rm}} = (1 - f)\dot{\varepsilon}_{\mathrm{fm}} \tag{27}$$

Combining Eqs 26 and 27 leads to

$$\dot{\varepsilon}_{\mathrm{c}}/\dot{\varepsilon}_{\mathrm{c}}^{\mathrm{rm}} = 1/[1 + f(4G_{\mathrm{m}}/3K_{\mathrm{m}})] \tag{28}$$

The theory predicts relatively small effects, with a general absence of stored elastic strain, contrary to conclusions based on other viscoelastic models [159, 160]. Viscoelastic sintering models in which large stored elastics strains arise are, however, not representative of densification driven by surface energy [161]. For volume fractions up to about 15% the Scherer treatment predicts the composite experimental densification rate fairly well for glass matrix systems, but significantly underestimates the effects of rigid inclusions at higher volume fractions. The agreement is less satisfactory for ceramic matrix systems. The most likely reasons are that compact/matrix particle packing is modified near inert inclusion in the powder compaction stage and, more importantly, that formation of rigid skeletal inclusion networks tend to form effectively obstructing densification [128, 162, 163]. This latter point is strongly supported by the significant difficulties in densification that are encountered when attempting to make fiber- or whisker-containing ceramic matrix composites by powder compaction routes.

4.1.6.2 SUPPORTED FILMS

Stresses that arise in films densifying on rigid substrates were analyzed by Scherer and Garino [164]. When particulate films on rigid substrates densify, a back stress will be generated by the invariant substrate, opposing densification parallel to the substrate surface. The stress is effectively a tensile stress that maintains strain compatibility with the substrate, subjecting the densifying film to simultaneous tensile creep. These stresses can be substantial. If the film is sufficiently thin, the stress distribution normal to the film surface can be considered uniform. The interface adhesion or shear strength must be sufficiently high to support the force balance. For a fixed interface strength a critical film thickness results beyond which the interface can no longer support the creep stress, resulting in interface failure, such as delamination. Typically, for sintering of particulate films on rigid substrates, this critical thickness is less than 40 μm, but can be much less when large densification strains or weak interfaces are involved [165]. For the sintering of sol–gel films, for example, the critical thickness is commonly less than 0.5 μm. An example of a cracked and delaminated sol–gel film after sintering is shown in Figure 4.1.27.

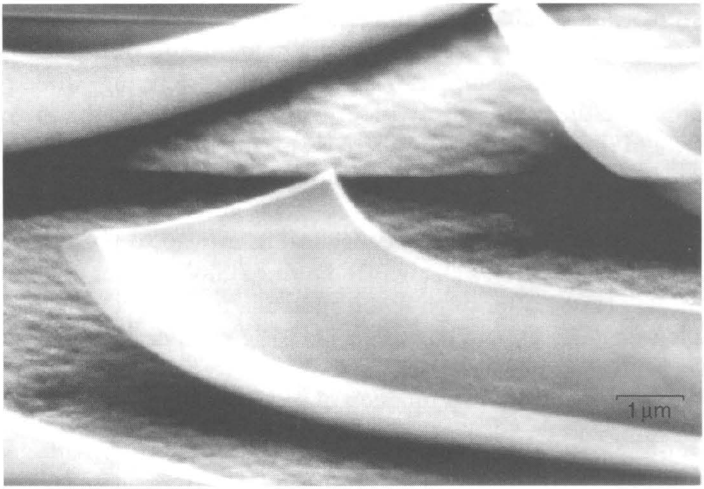

FIGURE 4.1.27 Delamination of a sintered zirconia thin film produced by sol–gel methods on a nanoporous (0.02 μm) alumina substrate (from Ref. [166]).

Failure by cracking can also be initiated in the film itself. Elastic film cracking occurs most readily during the drying stage, if the films are deposited by sol–gel or particulate colloidal methods. Using simple fracture mechanics concepts, a crack stability analysis again leads to a critical film thickness, in which the fracture toughness of the film is a determining factor. The treatments generally lead to a critical film thickness that is proportional to the square of the film fracture toughness. The fracture toughness of the films can, however, vary widely depending on their structure, and a critical thickness is therefore difficult to predict quantitatively. In general, a higher critical thickness results from better interface adhesion, reduction of strain-to-full-density (i.e. high green density), lowering of the creep viscosity relative to the densification viscosity, careful drying prior to densification, a uniform green structure, and maintaining low densification rates at low sintered densities. A factor that must also be considered for thin polycrystalline films is their dimensional stability. Instabilities enter when film grain sizes are larger than the film thickness, when grain boundary grooving can reach the film/substrate interface [167].

4.1.7 SINTERING PRACTICE

A wide variety of techniques have been developed to obtain dense ceramics with a desired microstructure and phase composition. In general, these methods involve a combination of a heating schedule and applied pressure. Heating schedules can be simple, as in isothermal sintering, or have a complex temperature–time relationship, as in rate-controlled sintering, while pressure may be applied either uniaxially, with or without a die, or by the surrounding gas. Control of the sintering atmosphere is also important, and precise control of oxygen [168] or nitrogen partial pressure as a function of temperature may in some cases be beneficial or essential [169]. Insoluble gases trapped in closed pores may obstruct final stages of densification or lead to post-densification swelling and, in these cases, a change of sintering atmosphere or vacuum sintering is indicated [170]. Atmosphere protection may also be provided by packing the sample in an appropriate powder [171]. The practice of sintering further includes a control of the particle characteristics, green compact structure, and consideration of chemistry as a function of processing conditions.

4.1.7.1 HEATING SCHEDULES

A general heating schedule is shown in Figure 4.1.28. Binder burnout, removal of volatiles such as water, and conversion of additives such as organometallics or polymers take place. Typically, the first hold temperature is, at most, a few hundred degrees centigrade. The heat-up rate should be carefully controlled, since it is quite possible that rapid heating causes boiling and evaporation of organic additives leading to specimen bloating or even shattering. Stage 2 can be included to promote chemical homogenization or reaction of powder components. Stage 3 represents the heat-up to the isothermal sintering stage 4, during which the majority of the densification and microstructure development takes place, which is then followed by a cool-down. An additional hold in stage 5,

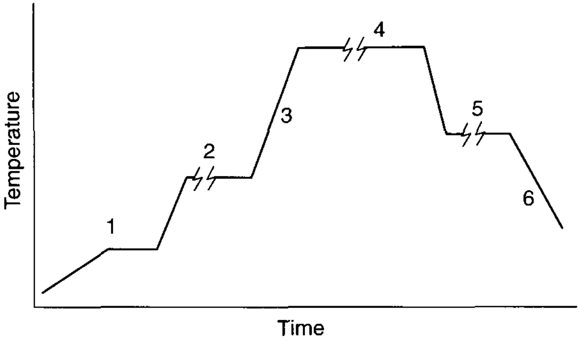

FIGURE 4.1.28 Generalized heating schedule.

prior to the final cool-down of stage 6, may also be included to relieve internal stresses or allow for precipitation or other reactions.

4.1.7.1.1 Isothermal Sintering

In isothermal sintering, perhaps better called isothermal-stage sintering, the temperature is increased monotonically to a sintering hold temperature and lowered to room temperature afterwards. The holding time is long compared to the heat-up time. This is the most common heating schedule. The heat-up times are limited by the sample size and by the thermal characteristics of the furnace. Heat-up times for large bodies can stretch over many hours, to avoid temperature gradients that could lead to cracking or to the formation of an outer dense layer on an incompletely densified core, as would result from differential densification.

During the heat-up phase of the isothermal sintering, significant densification and microstructural changes can take place, which all too often are ignored in sintering studies. Also, as a general rule, densification processes should be carried out significantly above the intended service temperature.

4.1.7.1.2 Constant Heating Rate Sintering

In this case, the sample is heated to a specified temperature at a controlled heating rate, and immediately cooled. Constant heating rate experiments may actually be simpler to analyze theoretically [24, 172] than the "isothermal" ones, because strict isothermal sintering is not possible. In practice, the use of constant heating rates is again limited by the sample size. High constant heating rates are then most useful in laboratory studies. Manipulation of the heating rate can be useful in the case where reactions take place during densification. For example, Boccaccini *et al.* [173] studied densification and crystallization of a glass powder in which densification was inhibited by crystallization at 1 K/min, but densification was complete prior to crystallization at 15 K/min.

Chu *et al.* [174] studied the microstructure and densification kinetics of ZnO over a wide range of constant heating rates. In general, higher heating rates lead to a finer grain size. The relative density versus temperature clustered in a fairly narrow band, for heating rates between 0.5 and 15 K/min. An interesting observation is that the derivative of the strain with respect to temperature for this range of constant heating rates falls on the same master curve. Lange [175] made a similar observation for alumina.

4.1.7.1.3 Multi-stage Sintering

Multi-stage sintering is frequently used in practice, sometimes introducing extended temperature plateaus or more complex temperature–time sequences

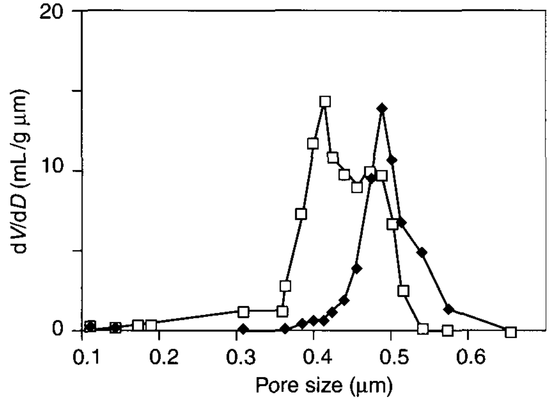

FIGURE 4.1.29 Pore size distribution narrowing after 50 h at 800°C for an alumina powder compact, determined by mercury porosimetry (from Ref. [177]).

in the heating schedule, with the purpose of achieving either specific chemical or microstructural features. An example of staged sintering, involving two separate peak temperatures in which the temperature is reduced between the stages is in the sintering of the ion-conducting ceramic sodium beta alumina [176]. Optimum results with respect to microstructure and strength were achieved in this case by reducing the sintering temperature by about 150°C after reaching the first peak temperature (about 1500°C).

A reduction in grain size and an increase in uniformity were also found by Lin *et al.* [177] and by Chu *et al.* [178] for MgO, Al_2O_3, and ZnO using a two-stage sintering technique. The first stage consisted of an extended hold at a temperature where shrinkage was 0.5–1% after 48 h. This temperature is readily found by running a dilatometery trace at constant heating rate. At the holding temperatures limited coarsening occurs that appears to have the effect of homogenizing the porous powder compact. Figure 4.1.29 shows the change in pore size distribution after limited coarsening for an alumina powder (AKP-50; Sumitomo America Corp.). Excessive coarsening should be avoided.

4.1.7.1.4 Rate-Controlled Sintering

In rate-controlled sintering, the densification rate is coupled with the temperature control of the sintering furnace in such a way as to keep the densification rate constant or limited [179, 180]. The result is a fairly complicated temperature history that at times approaches the staged sintering processes. While the underlying mechanisms are not fully understood, beneficial effects on microstructure have been reported in several instances, including where chemical reactions occur during densification [181, 182]. Manipulation of the sintering temperature is necessarily limited by the thermal impedance of the sintering furnace and by the size of the sample.

4.1.7.1.5 Fast-Firing

Ratio-controlled sintering and fast-firing are based on the principle of increasing the densification rate relative to the coarsening rate [183]. In ratio-controlled sintering, a temperature is selected that depends on the relative activation energies of these competing processes. This is shown schematically in Figure 4.1.30. The preferred sintering temperature is one where the densification rate is higher than the coarsening rate [184].

The most common situation is one where at higher temperatures densification rates are faster than coarsening rates. This leads to the process of fast-firing, in which the sample is taken to the high sintering temperature as rapidly as the system allows. The process can be particularly effective for thin walled tubes, for example, in rapid zone sintering where the ceramic piece is moved through a hot zone.

4.1.7.1.6 Microwave Sintering

Microwave heating is effective for heating more complex ceramic forms very rapidly [185]. Heating rates in excess of 1000°C/min can be achieved. In this method, the ceramic body, usually contained in non-absorbing or weakly absorbing insulation such as loose, non-conducting powder, is placed within a microwave cavity. A schematic of the method is shown in Figure 4.1.31.

The method is quite straightforward. It is even possible to use a simple consumer microwave oven to achieve densification of ceramic powder compacts

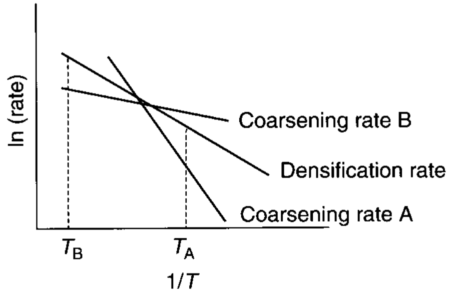

FIGURE 4.1.30 Possible relation of coarsening rates to densification rate. The preferred sintering temperatures T_A or T_B correspond to the coarsening rates A or B.

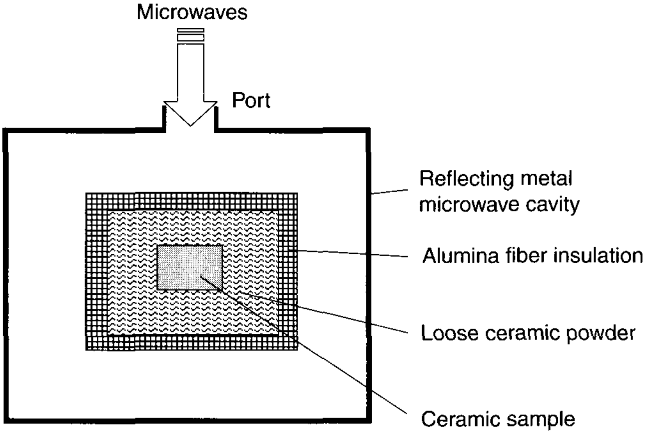

FIGURE 4.1.31 Schematic microwave sintering setup.

when properly insulated [186]. The shape of the ceramic body affects the local heating rates significantly and achieving sufficiently uniform heating can be difficult [187]. The microwave frequency plays a significant role in the temperature gradients that can develop within the ceramic body. High frequencies tend to heat the exterior of the sample more than the interior, and a combination of frequencies ranging between about 2.5 and 85 GHz has been proposed as providing more uniform heating [188]. Continuous microwave sintering has also been reported, in which samples are passed through the apparatus [189].

A variant of microwave sintering is one where the microwaves ignite a plasma that surrounds the ceramic part. Very high sintering rates can be achieved this way. The schematic of the method is shown in Figure 4.1.32. Johnson *et al.* [190] achieved full densification for tubular specimens by translating the tube at a rate of 25 mm/min through a plasma of about 50 mm in height. It is, as yet, not clear if the plasma itself enhances the densification rates in addition to the high temperature created by the plasma.

4.1.7.1.7 Plasma-Assisted Sintering

Several attempts have been made at increasing the heating rates, causing a need for various superlatives such as "superfast" or "ultrafast" sintering, by passing a DC current pulse through a powder compact contained in a graphite die, under an applied pressure of 30–50 MPa. This method has been called spark plasma sintering (SPS). A schematic of the method is shown in Figure 4.1.33. Specimen temperatures are difficult to assess in this method, and are usually

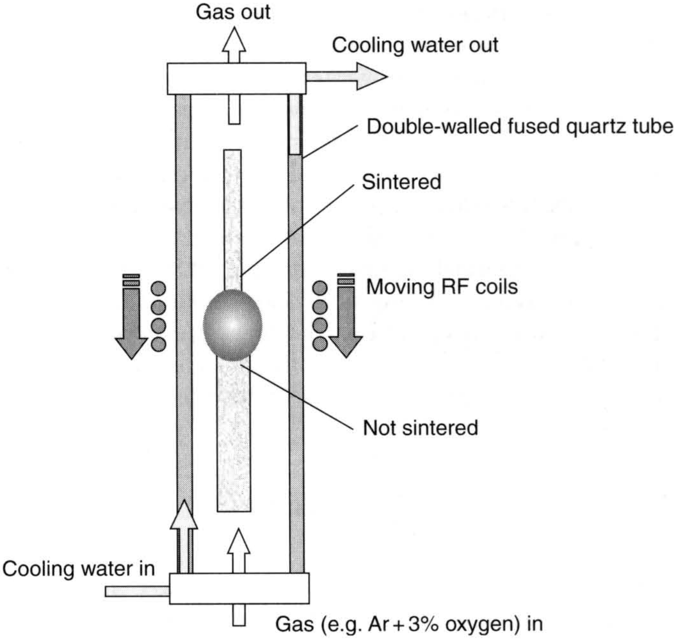

FIGURE 4.1.32 Schematic of plasma sintering setup.

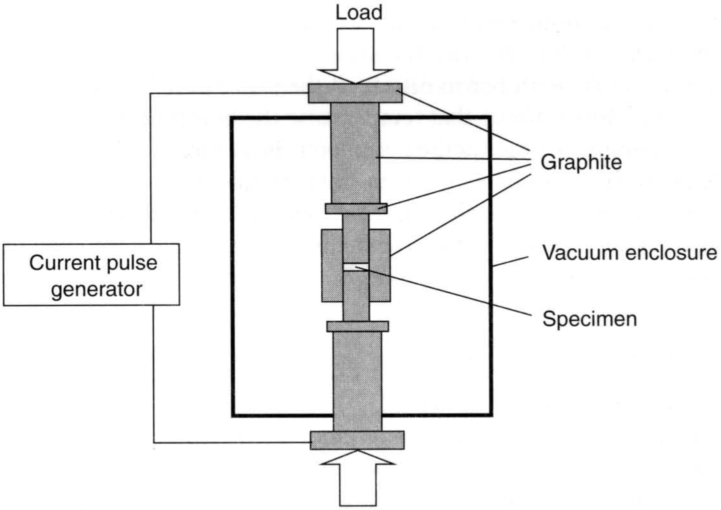

FIGURE 4.1.33 Schematic of a spark plasma sintering apparatus.

measured by optical pyrometry on the graphite die wall. Both the die and the specimen are heated by the current pulse. Heating rates of 600 K/min and more have been reported. The high heating rates are thought to be caused, in part, by spark discharges generated in the voids between the particles. Remarkably high densification rates may be achieved under such conditions, with minimal grain growth. This approach is particularly useful in producing dense ceramic bodies from nanosized powders [191, 192]. The specimen shapes that can be prepared by SPS are limited to simple slabs that can be contained in the compression die. A related method is a thermal explosive forming, in which a reactive mixture of components, for example, Ti and C, is heated up in a die, and then ignited by passing an electrical current pulse. The process may perhaps be regarded as a self-propagating high-temperature synthesis under pressure. Formation of dense boride, nitride, and carbide composites has been reported [193].

4.1.7.2 PRESSURE-ASSISTED SINTERING

4.1.7.2.1 Hot pressing

Hot pressing is a convenient laboratory method for preparing dense samples [194]. Heat and pressure are applied to a sample contained typically in a high-strength graphite die, at applied pressures around 50 MPa. The die wall thickness is approximately equal to the sample diameter if high-strength graphite [195] is used. Other die material such as aluminum oxide, silicon carbide, or dies confined by an outer metal or fiber-wound mantle are also used in rare cases. Reaction of the graphite die with the sample can be decreased by spray coating the inside of the die with boron nitride, if the processing temperature remains below about 1350°C. Above that temperature the boron nitride can react with graphite. Boron nitride sprays are commercially available [196]. Lining of the graphite die with graphite foil is also useful for prolonging the die life. Multiple plate-shaped samples may be hot pressed together, using graphite spacers.

An interesting variant allowing for shape flexibility was developed by Lange *et al.* [197]. In this method, the sample is packed in coarse powder in the hot pressing die, developing a roughly isostatic pressure on the work piece. A schematic of the standard process is shown in Figure 4.1.34. More complex systems have also been developed, for example, a multi-bore machine for hot pressing nuclear reactor pellets [198].

In a typical hot pressing process, a moderate pressure is applied form the start, 10–20 MPa. Upon reaching the sintering temperature the pressure is increased to maximum. An applied pressure is usually maintained during the cool-down period as well. A schematic of the thermomechanical treatment is shown in Figure 4.1.35.

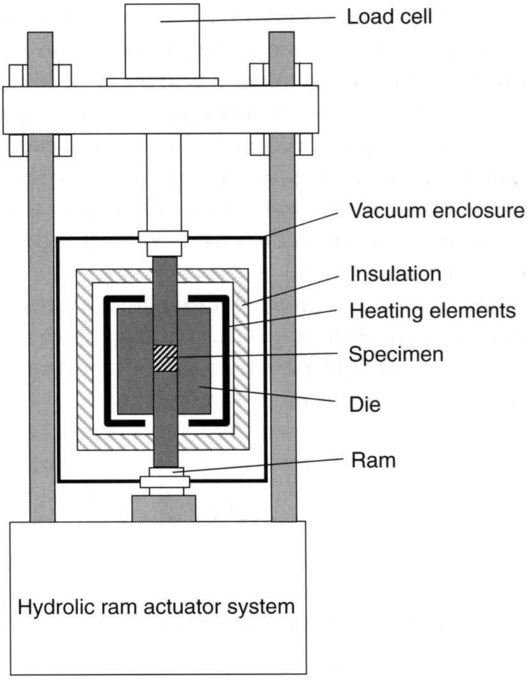

FIGURE 4.1.34 Schematic of the hot pressing process.

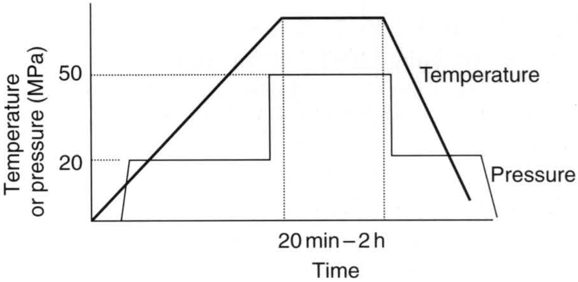

FIGURE 4.1.35 Schematic temperature/pressure schedule for hot pressing with a high-strength graphite die.

If no reliable temperature measurement is available, it is possible to follow the ram displacement as the temperature is increased. An appropriate sintering temperature is then reached when the rate of the ram displacement rapidly increases to indicate a projected full densification in 20–30 min. Hot pressing is less effective for very fine powder that is well compacted prior to hot pressing. For submicron powders the intrinsic sintering stress can be significantly in excess of what the hot-press die can tolerate, and the applied stress then appears less effective. Benefits may still be derived from the applied pressure when it can assist in the rearrangement process or in the collapsing of large pores. Some guidance for selecting the appropriate hot pressing temperature may be obtained form pressure sintering maps [199], although trial-and-error is more reliable. In case full densification is difficult to achieve, additives can be used similar to the free sintering method.

As a result of the significant uniaxial strain in hot pressing, texture may develop in the finished part. Trapping of insoluble gases in residual pores may cause swelling of the ceramic at elevated service temperatures. This can be avoided by hot pressing in vacuum.

Reactive hot pressing has also been used successfully [200, 201]. Densification is more readily achieved in this case compared to unconfined sintering. Related to reactive hot pressing is hydrothermal hot pressing. In this method, powders are compacted under hydrothermal conditions. The powder is essentially compacted inside an autoclave at temperatures between 100 and 350°C. The ram design should allow for fluid to leave the sample. Materials such as hydroxyapatite [202] and amorphous titania [203] have been compacted this way.

4.1.7.2.2 Sinter Forging

Sinter forging is similar to hot pressing, but without confining the sample in a die, as shown in Figure 4.1.36. Uniaxial strains are, as a result, significantly larger than in die hot pressing [204]. For fine powders use can be made of possible superplastic deformation modes during sinter forging. During the process, the strain rate has to be limited to avoid damaging the sample [205].

4.1.7.2.3 Hot Isostatic Pressing (HIPing)

A schematic of the equipment is shown in Figure 4.1.37 [206]. In this method, developed around 1955, the pre-consolidated powder is tightly enclosed in a glass or metal container, sealed under vacuum and positioned in the pressure vessel. Alternatively, the sample can be pre-densified to closed porosity by traditional sintering, after which a canister is not needed in subsequent HIPing. A compressor introduces inert gas pressure, and the sample is heated to the sintering temperature, which may be up to 2000°C. During this time the gas pressure rises further to as much as 30 000 psi, and the container collapses around the sample, transmitting the isostatic pressure to the sample. Commercial hot

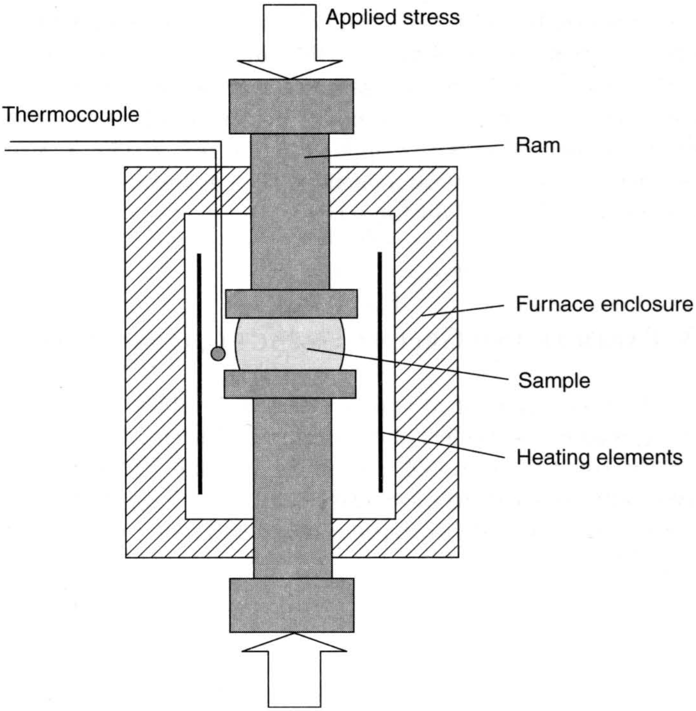

FIGURE 4.1.36 Schematic setup for sinter forging.

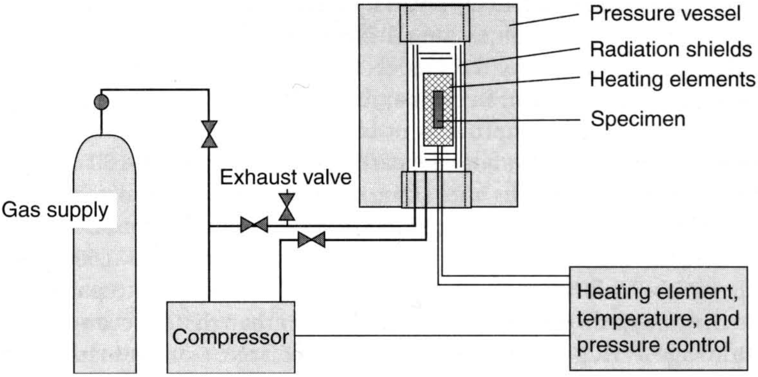

FIGURE 4.1.37 Schematic of hot isostatic pressing equipment.

isostatic presses may have internal chamber diameters approaching 1 m. Heating elements are typically graphite, molybdenum, tungsten, or tantalum. The quality of the ceramics produced by hot isostatic pressing is perhaps the highest obtainable by any other pressure method, since externally heated dies cannot withstand the pressure that can be applied by the HIP. HIPing is also used to recondition parts in which internal damage, such as resulting from fatigue or creep, may have accumulated during service.

4.1.7.3 PARTICLE AND GREEN COMPACT CHARACTERISTICS

While the sintering behavior of real powders is considerably more complex than that assumed in the models, the sintering theory clearly indicates the key parameters that must be controlled to optimize sintering. The key factors are the particle size of the powder and the particle packing in the green body but other characteristics, such as size distribution, shape and structure of the particles, can also exert a significant influence.

4.1.7.3.1 Particle Size

The matter transport rates for the solid-state sintering mechanisms depend strongly on the particle size of the powder (Eqs 6 and 7). Assuming sintering conditions (e.g. the heating schedule) where the densifying mechanisms dominate, then the rate of densification is predicted to vary as $1/G^m$, where G is the particle size, and the exponent $m = 4$ for grain boundary diffusion and $m = 3$ for lattice diffusion. Thus, reduction of the particle size provides an important method for speeding up sintering. This is illustrated by the data shown in Figure 4.1.38 for CeO_2 powder compacts with three different particle sizes [207, 208]. Because of packing difficulties, the observed sintering rate is lower than that predicted by the models but the enhancement of the rate with decreasing particle size is still considerable.

A consequence of the improvement in the sintering rate is the use of lower sintering temperatures. Nanoscale particles (less than 50–100 nm in size) exhibit large reductions in the sintering temperature. From the data in Figure 4.1.38, isothermal sintering of the 10-nm particles can be achieved at less than ~1150°C, compared to a sintering temperature of 1500–1600°C for the 1 μm particles. Unfortunately, nanoscale particles are prone to packing problems so that the green density is commonly lower than that for coarser powders. The shrinkage during sintering can therefore be large. Contamination can also be a problem due to the large surface area of the powder. The removal of surface impurities, such as hydroxyl groups, from the surface of nanoscale particles can

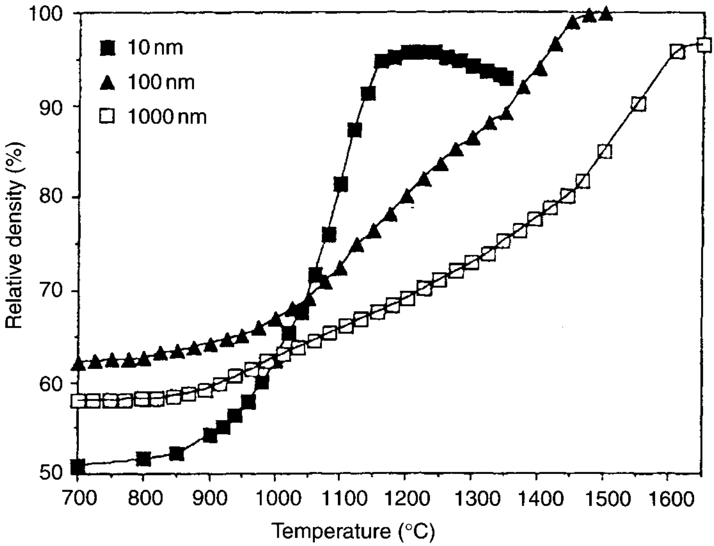

FIGURE 4.1.38 Effect of particle size on the sintering of CeO_2 powder compacts during constant heating rate sintering (10°C/min) in an oxygen atmosphere (from Ref. [207]).

also be difficult. Decomposition during sintering can lead to trapped gases in the pores that can limit the final density, as seen in Figure 4.1.38 for the 10-nm particles.

4.1.7.3.2 Particle Size Distribution

The solid-state sintering models generally assume that the particles are monodisperse but a particle size distribution can have significant effects on sintering. Coble [209] modeled the initial-stage sintering of a linear array of particles with different sizes and found that an equivalent particle size, considerably smaller than a conventional average size, can be used to account for the shrinkage. The results also show that the sintering rates of binary mixtures of particles are intermediate between those for the end-member sizes. A simple rule of mixtures has, in fact, been proposed to describe the sintering data of binary mixtures of alumina powders where the coarser phase is relatively inactive [210, 211]. Commonly, differential densification between the coarser phase and the finer phase coupled with interactions between the particles in the coarser phase can severely inhibit densification (see Chapter 6).

The use of mixtures of discrete particle sizes or a wide distribution of particle size can result in an increase in the packing density (because the finer particles fit into the interstices of the larger particles), so that the shrinkage required for

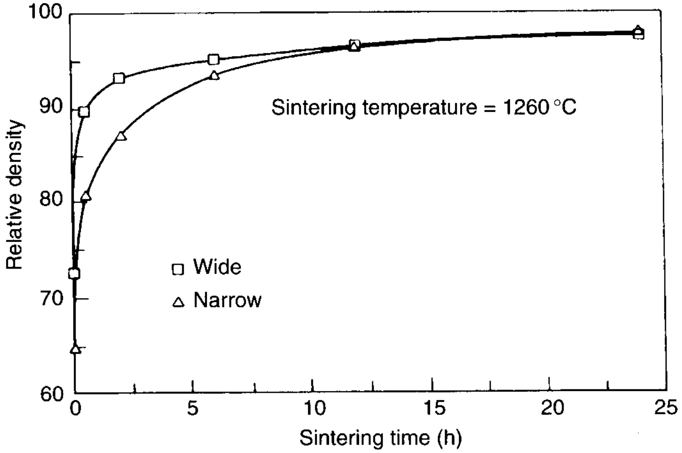

FIGURE 4.1.39 Effect of particle size distribution on the sintering of slip cast Al_2O_3 powder compacts prepared from wide and narrow size distribution powders having the same median particle size (from Ref. [228], with kind permission of American Ceramic Society).

complete densification is reduced. This reduction in the shrinkage is important in industrial sintering of large objects. As shown in Figure 4.1.39, increasing the width of the particle size distribution has a benefit in the early stages of sintering due to the presence of the fine powders with the higher driving force for sintering [212–214]. The behavior in the later stages of sintering depends critically on the particle packing of the green body. For heterogeneous packing, an increase in the width of the particle size distribution is expected to enhance the detrimental effects of differential densification and grain growth (due to the enhanced driving force arising from the size difference) so that the final density may decrease. However, if the particle packing is homogeneous, with small pores of narrow size distribution, a high final density can be achieved regardless of the width of the initial particle size distribution (Fig. 4.1.39), emphasizing the importance of the pore structure in sintering.

4.1.7.3.3 Particle Shape and Particle Structure

Particle shape influences sintering primarily through its effect on the packing of the green body. Deviations from the spherical or equiaxial shape lead to a reduction in the packing density and packing uniformity, resulting in a reduction of densification. Compacts of acicular (or elongated) particles can, however, be sintered to high density if the particles are aligned and the packing is homogeneous, as demonstrated for acicular Fe_2O_3 particles [215]. Some solids maintain or develop faceted shapes during sintering [216–219] but the effects of shape are often complicated by other factors (e.g. packing, influence of composition).

Particles used in sintering are commonly dense, discrete units that can either be polycrystalline or a single crystal. Polycrystalline particles of Y_2O_3-stabilized ZrO_2 have been observed to sinter faster than single-crystal particles and this has been attributed to the larger number of grain boundaries contributing to mass transport [220]. A problem is that the single crystals and the polycrystalline particles have different Y_2O_3 content so that the structural effects cannot be clearly separated from compositional effects. Spherical, monodisperse particles synthesized by the Stober process consist of an aggregate of much finer particles (Fig. 4.1.40). The influence of this particle substructure on sintering has been well characterized by Edelson and Glaeser [221, 222]. For TiO_2, heating to 700°C produces sintering of the fine particles in the spheres and conversion to rutile so that the spheres consist of one to three grains by the time the spheres start to sinter at ~1000°C.

4.1.7.3.4 Particle Packing

For enhanced sintering rates and the attainment of high density, the particles must be homogeneously packed with a high packing density. These

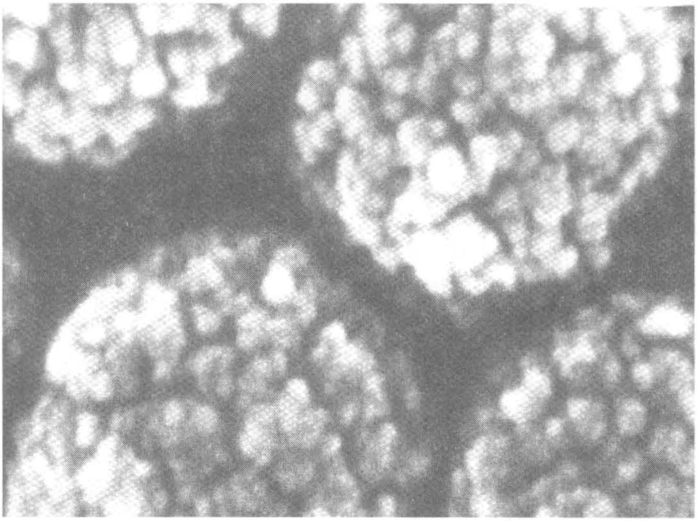

FIGURE 4.1.40 High-resolution SEM micrographs showing the substructure of monodisperse TiO_2 particles prepared by the Stober process. The spherical particles (~0.35 μm) consist of an aggregate of much finer particles (~10 nm) (courtesy of A. M. Glaeser).

packing characteristics produce fine, uniform pores with a low pore coordination number corresponding to the shrinking pore in Figure 4.1.3. Furthermore, the number of particle contacts is maximized, thereby providing many grain boundaries and short diffusion paths for rapid matter transport into the fine pores. Rhodes [223] provided a clear demonstration of these principles in a study of the sintering of Y_2O_3-stabilized ZrO_2. Using a fine powder (crystallite size ~10 nm) synthesized by the hydrolysis of alkoxides, he prepared a suspension and allowed the agglomerates to settle. The fine particles in the supernatant were then used to prepare compacts by gravitational settling in a centrifuge. After drying the compact had a density of 0.74 of the theoretical density. As shown in Figure 4.1.41, sintering for 1 h at 1100°C produced almost complete

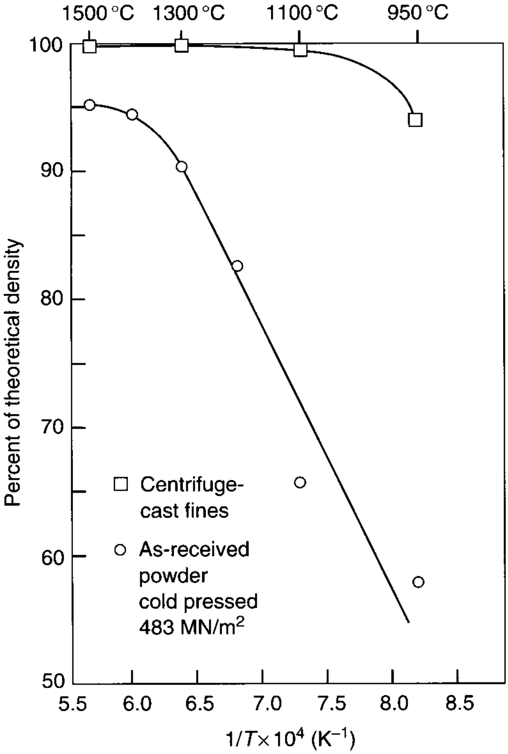

FIGURE 4.1.41 Effect of particle packing on the sintering of Y_2O_3-stabilized powder compacts after 1 h at various temperatures. The compact with the more homogeneous microstructure (formed by centrifugal casting of fine, agglomerate-free particles) reaches a significantly higher density than a compact formed by die-pressing the agglomerated, as-received powder (from Ref. [223], with kind permission of American Ceramic Society).

densification. In comparison, compacts prepared by die-pressing of as-received, agglomerated powder reached a density of only 0.95 of the theoretical after sintering for 1 h at 1500°C.

Barringer and Bowen [224, 225] developed a processing approach based on the uniform packing of monodisperse, spherical particles. While rapid sintering was achieved at considerably lower temperatures, the compacts could not be sintered to full density (the residual porosity was ~5%). A problem is that the uniform consolidation of monodispere particles leads to the formation of small regions with three-dimensional, *ordered* packing (typical of the packing in crystals), referred to as *domains*, which are separated by packing flaws (voids) at the domain boundaries. The faster sintering of the ordered regions, when compared to the domain boundaries, leads to differential stresses that cause enlargement of the voids. These voids correspond to the growing or stable pores in Figure 4.1.3.

Liniger and Raj [226] have suggested that dense, *random* packing of particles with a distribution of sizes may provide an alternative ideal packing geometry for enhanced sintering. When compared to the ordered packing of monodisperse particles, the random structure would be less densely packed than the domains but the fluctuations in density should be less severe, leading to homogeneous sintering and the reduction of flaw generation due to differential sintering. Homogeneously packed Al_2O_3 green bodies formed by colloidal processing of fine powders have, in fact, been sintered to almost full density at temperatures as low as ~1200°C [227, 228].

It is important to appreciate the implications of deviating from the ideal structure because most practical sintering, particularly for industrial applications, are not performed with an ideal system of homogeneous, densely packed, fine particles. A key problem is *differential densification*, which may lead to enlargement of the voids or even the generation of crack-like voids in the less dense regions (Figure 4.1.42). The large voids correspond to the growing or stable pore in Figure 4.1.3 so that they limit densification. The effects of differential densification on particle rearrangement in two-dimensional packing of spheres have been well characterized by Weiser and De Jonghe [229] and by Exner [230]. Another factor is that the denser regions can support grain growth: enhanced normal grain growth starts at an earlier point during sintering, thereby increasing the probability for the initiation of abnormal grain growth.

A relevant question is whether the effects of differential densification can be corrected or reversed during sintering. Lange [231] has proposed that a limited amount of normal grain growth is beneficial for sintering in that it reduces the pore coordination number of the pores. This means that grain growth can convert the growing pore with a high coordination number in Figure 4.1.3 to a shrinking pore with low coordination number. Support for Lange's suggestion

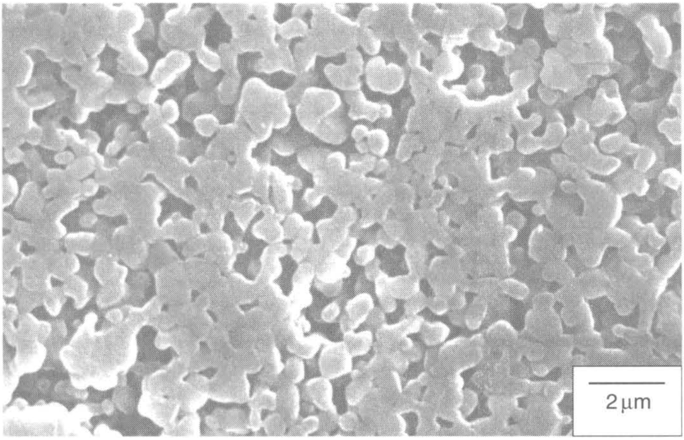

FIGURE 4.1.42 Differential densification during the sintering of an Al_2O_3 powder compact formed by die-pressing, leading to the development of denser and less dense regions.

was observed in the sintering studies of Lin *et al.* [232] on heterogeneously packed MgO powder. Grain growth can, however, provide only a short-term benefit because the increase in the diffusion distance eventually produces a significant reduction in the overall sintering rate [233]. For nanoscale CeO_2 powders, Chen [234] has suggested a mechanism of coarsening coupled with repacking of the porous network to explain the sintering of compacts with low green density to almost full density.

As described earlier, De Jonghe and coworkers [177, 178] have demonstrated that a two-step sintering approach, which involves an initial pre-coarsening step prior to densification, leads to some improvement of the microstructural homogeneity during sintering and to corresponding microstructural benefits in the sintered material.

While the effects of heterogeneous packing can be alleviated to some extent during sintering, the benefits may not be as compelling as may be required in most systems so that a more realistic approach would be based on optimizing the particle packing in the green body.

4.1.7.3.5 Effect of Green Density on Sintering

The green density of the powder compact is an important parameter in sintering. Higher green density leads a decrease in the shrinkage during sintering (due to the reduced pore volume) and to an increase in the sintering stress due to the reduced pore size [37]. Several studies have shown a correlation between the sintered density and the green density: the sintered density is observed to decrease with green density for green density values below 55–60% of the theoretical value [235–237].

Commonly, compacts with green densities lower than 40–45% of the theoretical value are difficult to sinter to high density. Increasing green density is found to delay the onset of enhanced grain growth during the later stages of sintering [238]. These trends in the data can be explained in terms of the higher probability for the occurrence of pores with large coordination numbers with decreasing green density coupled with the enhancement of differential densification. In general, the benefits of higher green density for sintering are clear, so optimization of the green density would form a useful approach. However, in some systems a lower green density does not necessarily influence the ability to attain a high sintered density, as exemplified by the data in Figure 4.1.43 for ZnO. Even with a low green density, compacts of some nanoscale powders can also be sintered to high density; as described earlier, CeO_2 powders with a green density as low as 20% which have been sintered to almost full density [239].

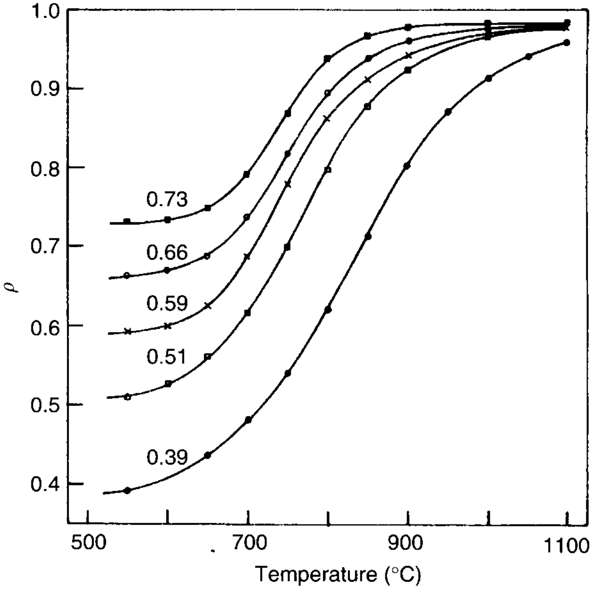

FIGURE 4.1.43 Effect of green density on the sintering of ZnO powder compacts during constant heating rate sintering (5°C/min) to 1100°C showing that for this powder, the final density is almost independent of the green density for a wide range of green density values (0.39–0.73) (from Ref. [37]).

4.1.7.4 CHEMISTRY CONSIDERATIONS

The sintering atmosphere can have a decisive effect on the microstructural evolution, particularly in the case of advanced ceramics that must meet exacting property requirements. Atmosphere is not directly considered in the sintering models but the theories can provide a basis for understanding the phenomena arising from the atmosphere conditions. Both physical phenomena (e.g. the atmospheric gas trapped in the pores) and chemical phenomena (e.g. volatility, ionic oxidation state and defect chemistry) are involved.

4.1.7.4.1 Gases in Pores

In the final stage of sintering, gas from the atmosphere (or from volatile species in the solid) is trapped in the pores when the pores pinch off and become isolated. Further sintering is influenced by the solubility of the gas atoms in the solid, as has been demonstrated by Coble [170] in the sintering of Al_2O_3. Coble found that MgO-doped Al_2O_3 can be sintered to theoretical density in O_2 or H_2, which can diffuse out to the surface of the solid, but not in air, N_2, He, or Ar, which have a limited solubility in Al_2O_3.

If it has a high solubility in the solid, the gas does not have a significant influence on sintering. For an insoluble gas, application of the gas laws shows that sintering stops when a limiting porosity, P_L, is reached, as given by

$$P_L = P_0 \left(\frac{p_0 r_0}{2\gamma_{sv}} \right)^{2/3} \tag{29}$$

where p_0 is the pressure of the sintering atmosphere, P_0 and r_0 are the porosity and radius, respectively, of the pores (assumed spherical in shape) when they become isolated, and γ_{sv} is the specific energy of the solid/vapor interface. According to Eq. 29, the limiting density is controlled essentially by the pressure of the gaseous atmosphere and by the radius of the pores when they become isolated. If practical, sintering in vacuum and homogeneous packing of fine particles (giving fine pores) can improve the final density.

When coarsening occurs with a slightly soluble or insoluble gas trapped in the pores, pore coalescence leads to a phenomenon referred to as *bloating*, whereby the density of the body starts to decrease, as illustrated in Figure 4.1.44. Bloating is also a common occurrence when relatively dense ceramics, previously hot pressed in a carbon die (or furnace), are annealed in an oxidizing atmosphere [240]. Oxidation of carbonaceous impurities leads to the generation of a gas that provides the pressure for the expansion.

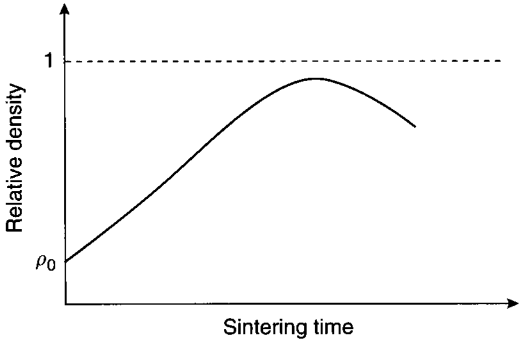

FIGURE 4.1.44 Schematic diagram illustrating the phenomenon of bloating produced by coarsening with gas-filled pores. The density decreases with time after reaching a maximum value.

4.1.7.4.2 Vapor transport

The heating schedule, as described earlier, provides an important process parameter for controlling the relative rates of the densifying and coarsening mechanisms. Readey and coworkers [242–244] have demonstrated how enhanced vapor transport, produced by sintering in a reactive atmosphere, can provide another key process variable for microstructure control. For example, vapor transport in Fe_2O_3 can be produced by the introduction of HCl gas into the atmosphere:

$$Fe_2O_3\ (s) + 6HCl\ (g) \rightarrow Fe_2\,Cl_6\ (g) + 3H_2O\ (g) \qquad (30)$$

Densification decreases as the HCl pressure and the amount of vapor transport increases, and stops when the HCl pressure reaches values greater than 10^{-2} MPa. As shown in Figure 4.1.45, the decrease in densification is caused by particle coarsening. Water vapor in the atmosphere has also been shown to produce modifications in the densification/coarsening ratio [245–247].

4.1.7.4.3 Volatilization and Decomposition

For some powder compositions (e.g. sodium β-alumina and lead-based ferroelectric ceramics), evaporation of volatile components can occur during sintering, thereby making it difficult to control the composition and the microstructure of the sintered material. Evaporation of PbO in lead-based electroceramics can be represented as [248, 249].

$$PbO\ (s) \rightleftarrows PbO\ (g) \rightleftarrows Pb\ (g) + \tfrac{1}{2}O_2 \qquad (31)$$

Lead is poisonous so that, in addition to controlling lead loss, the evaporated lead must be contained. In practice, this is achieved by surrounding the sample

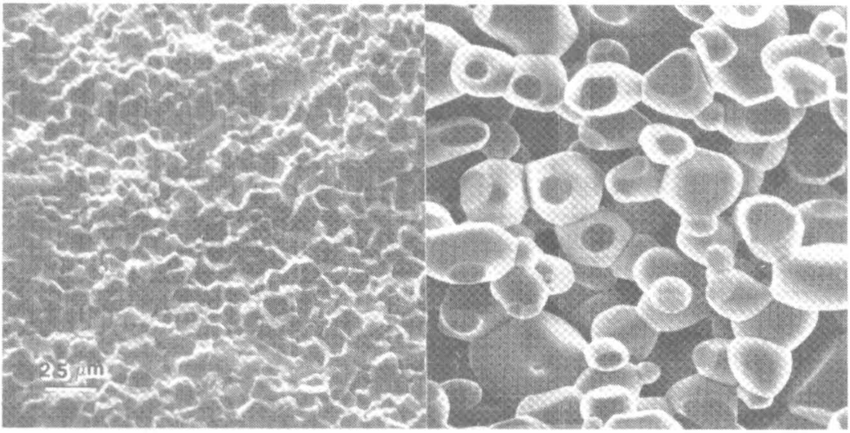

FIGURE 4.1.45 Scanning electron micrographs of fractured surfaces of Fe_2O_3 powder compacts sintered for 5 h in air (left) and in 10% HCl (right) (courtesy D. W. Readey).

with lead-based powder compositions (e.g. $PbZrO_3$ and PbO for lead zirconate–titanate samples) to provide a positive vapor pressure in a closed alumina crucible [171].

Silicon nitride shows significant decomposition at the high temperatures (1700–1800°C) required for its densification. The decomposition reaction can be written as

$$Si_3N_4 \rightleftarrows 3Si\ (g) + 2N_2\ (g) \tag{32}$$

The vapor pressure of the N_2 gas generated by the decomposition is $\sim$0.1 atm at the sintering temperature so that considerable weight loss can occur if the decomposition is not controlled. One solution is to surround the sample with a powder of the same composition in a closed graphite crucible under N_2 gas at normal atmospheric pressure. A better method involves raising the N_2 gas pressure in the sintering atmosphere (to values of 10–20 atm or higher) so that the reaction in Eq. 32 is driven to the left [250].

4.1.7.4.4 Oxidation State

The sintering atmosphere influences the oxidation state of certain cations, particularly those of the transition elements (e.g. chromium), and control of the oxidation state has been shown to have a significant effect on the densification of chromium-containing oxides [168, 251–253]. Figure 4.1.46 shows the porosity of three chromites as a function of oxygen partial pressure in the sintering

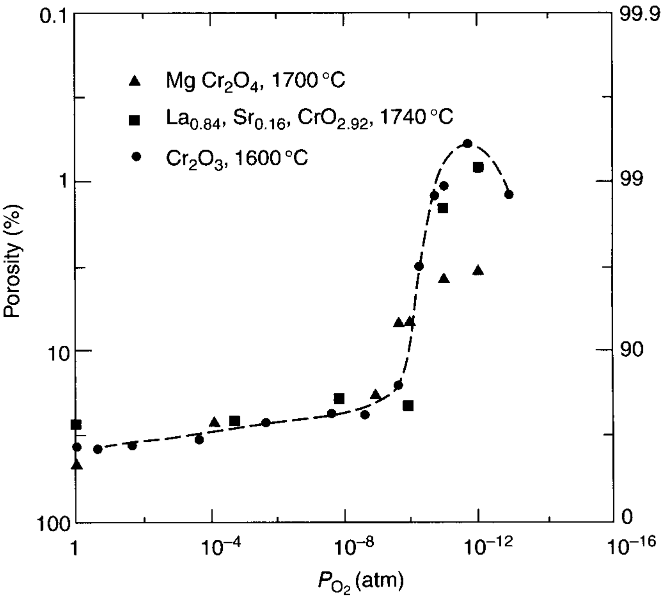

FIGURE 4.1.46 Dependence of porosity (or density) of sintered chromites on oxygen partial pressure in the sintering atmosphere (courtesy of H. U. Anderson).

atmosphere after sintering for 1 h at temperatures ranging from 1600–1740°C. The chromites show little densification if the oxygen partial pressure is greater than ~10^{-8} atm. However, densities of ~99% of the theoretical value can be obtained by sintering in an oxygen partial pressure of ~10^{-12} when the Cr ion is stabilized in its trivalent state (as Cr_2O_3). At higher oxygen partial pressure, Cr_2O_3 becomes unstable and vaporizes as CrO_2 or CrO_3. The high vapor pressure enhances evaporation/condensation processes, leading to neck growth and coarsening but little densification. The dramatic effects of oxidation state control observed for the chromites have not been repeated in other ceramic systems so that the approach sees limited applicability.

When compared to the undoped material, the use of TiO_2 as a dopant [254] allows the densification of Cr_2O_3 at a higher oxygen partial pressure (10^{-1} atm) and at a lower temperature (1300°C). It was suggested that the Ti^{4+} ions replace the chromium ions that are in an oxidation state greater than 3, thereby suppressing the formation of the volatile CrO_2 and CrO_3. The use of the TiO_2 dopant has also been claimed to produce chromium vacancies, leading to an enhancement of the sintering rate.

Atmosphere control is particularly important in the sintering of ferrites for magnetic devices, such as manganese zinc ferrite and nickel zinc ferrite [255].

In addition to limiting the evaporation of zinc, the atmospheric conditions must also give the right concentration of ferrous iron in the sintered ferrite for achieving the desired magnetic properties. This is commonly done by first sintering in an atmosphere of high p_{O_2} (0.3–1.0 atm) to minimize the evaporation of zinc, followed by annealing at a lower temperature in a low p_{O_2} atmosphere (10–100 ppm) to give the desired concentration of ferrous iron.

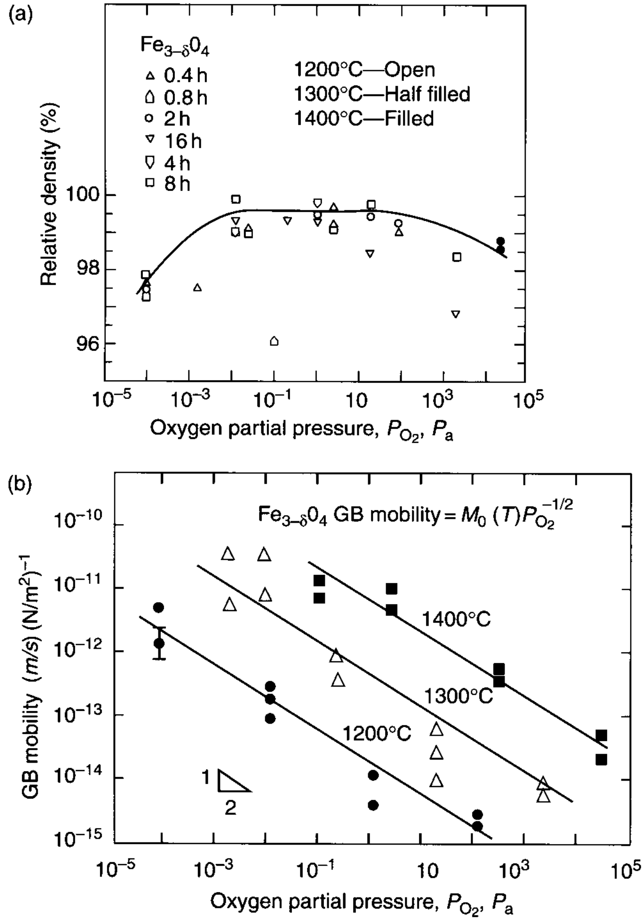

FIGURE 4.1.47 Data for (a) the relative density and (b) the boundary mobility as a function of the oxygen partial pressure in the atmosphere during the sintering of Fe_3O_4 powder compacts under the conditions of time and temperature indicated (from Ref. [257], with kind permission of American Ceramic Society).

4.1.7.4.5 Defect Chemistry and Stoichiometry

The sintering behavior of the highly stoichiometric oxides (e.g. Al_2O_3 and ZrO_2) shows almost no dependence on the oxygen partial pressure (p_{O_2}) in the atmosphere. For other ceramic oxides, particularly the transition metal oxides, the p_{O_2} can change the concentration and type of lattice defects and, hence, the stoichiometry of the compound [11, 12]. The sintering of these oxides would therefore be expected to depend significantly on the p_{O_2} of the atmosphere. Because they have a significantly larger ionic radius than most cations, the oxygen ions are often less mobile. Thus, an atmosphere that produces an increase in the oxygen vacancy concentration may enhance sintering. In practice, it is often difficult to separate the influence of defect chemistry and stoichiometry from the influence of changes in the non-densifying mechanisms (e.g. vapor transport and surface diffusion) brought about by the change in the atmosphere.

The influence of stoichiometry has been well demonstrated by Reijnen [256] in the sintering of $NiFe_2O_4$ and $NiAl_2O_4$. Densification is severely retarded for powder compositions with an excess of Fe or Al. This behavior was explained in terms of a reduction in the oxygen vacancy concentration. Figure 4.1.47 shows the densification and grain growth behavior of Fe_3O_4 as a function of p_{O_2} at three different temperatures [257]. While the type and concentration of the lattice defects may be expected to vary over the wide p_{O_2} range, the sintered density is insensitive to the atmosphere. However, the p_{O_2} has a significant effect on the grain growth: high p_{O_2} leads to small grain size whereas the grain size is much larger at low p_{O_2}. While the data cannot be fully explained, it has been suggested that oxygen lattice diffusion controls the pore mobility. Oxygen lattice diffusion is faster at lower p_{O_2}, so an increase in the pore mobility will give a faster grain growth rate if the boundary mobility is controlled by the pore motion (pore control in Figure 4.1.12).

REFERENCES

1. Evans, J. W., and De Jonghe, L. C. (1991). *The Production of Inorganic Materials*, New York: Macmillan.
2. Rahaman, M. N. (1995). *Ceramic Processing and Sintering*, New York: Marcel Dekker.
3. German, R. M. (1996). *Sintering Theory and Practice*, New York: Wiley.
4. De Jonghe, L. C., and Rahaman, M. N. (1988). Sintering stress of homogeneous and heterogeneous powder compacts. *Acta Metall.* 36: 223–229.
5. Raj, R. (1987). Analysis of the sintering pressure. *J. Am. Ceram. Soc.* 70: C210–C211.
6. Howard, R. E., and Lidiard, A. B. (1964). Matter transport in solids. *Rept. Progr. Phys.* 27: 161–240.
7. Ruoff, A. L. (1965). Mass transfer problems in ionic crystals with charge neutrality. *J. Appl. Phys.* 36: 2903–2907.

8. Readey, D. W. (1966). Mass transport and sintering in impure ionic solids. *J. Am. Ceram. Soc.* **49**: 366–369.
9. Gordon, R. S. (1973). Mass transport in the diffusional creep of ionic solids. *J. Am. Ceram. Soc.* **56**: 147–152.
10. Coble, R. L., and Cannon, R. M. (1978). Current paradigms in powder processing. *Mater. Sci. Res.* **11**: 151–170.
11. Kroeger, F. A. (1964). *The Chemistry of Imperfect Crystals*, Amsterdam: North Holland Publishing Co.
12. Kofstad, P. (1972). *Nonstoichiometry, Diffusion, and Electrical Conductivity in Binary Metal Oxides*, New York: Wiley.
13. Brook, R. J. (1972). Effect of TiO_2 on the initial sintering of Al_2O_3. *J. Am. Ceram. Soc.* **55**: 114–115.
14. Harmer, M. P. (1984). Use of solid solution sintering additives in ceramic processing. *Adv. Ceram.* **10**: 679–691.
15. Brook, R. J. (1988). Additives and the sintering of ceramics. *Sci. Sintering* **26**: 115–118.
16. Kingery, W. D., and François, B. (1967). Sintering of crystalline oxides, I. Interactions between grain boundaries and pores, *Sintering and Related Phenomena*, pp. 471–498, Kuczynski, G. C., Hooton, N. A., and Gibbon, G. F., eds., New York: Gordon & Breach.
17. Exner, H. E. (1979). Principles of single phase sintering. *Rev. Powder Metall. Phys. Ceram.* **1**: 1–251.
18. Coblenz, W. S., Dynys, J. M., Cannon, R. M., and Coble, R. L. (1980). Initial stage sintering models: a critical analysis and assessment, *Sintering Processes*, pp. 141–157, Kuczynski, G. C., ed., New York: Plenum.
19. Coble, R. L. (1961). Sintering of crystalline solids, I. Intermediate and final stage diffusion models. *J. Appl. Phys.* **32**: 787–792.
20. Coble, R. L. (1967). Mechanisms of densification during hot pressing, *Sintering and Related Phenomena*, pp. 329–347, Kuczynski, G. C., Hooton, N. A., and Gibbon, G. F., eds., New York: Gordon & Breach.
21. Coble, R. L. (1970). Diffusion models for hot pressing with surface energy and pressure effects as driving forces. *J. Appl. Phys.* **41**: 4798–4807.
22. Herring, C. (1950). Effect of change of scale on sintering phenomena. *J. Appl. Phys.* **21**: 301–303.
23. Song, H., Coble, R. L., and Brook, R. J. (1984). The applicability of Herring's scaling law to the sintering of powders. *Mater. Sci. Res.* **16**: 63–79.
24. Johnson, D. L. (1969). New method of obtaining volume, grain boundary, and surface diffusion coefficients from sintering data. *J Appl. Phys.* **40**: 192–200.
25. Bross, P., and Exner, H. E. (1979). Computer simulation of sintering processes. *Acta Metall.* **27**: 1013–1020.
26. Svoboda, J., and Riedel, H. (1995). New solution describing the formation of interparticle necks in solid-state sintering. *Acta Metall. Mater.* **43**: 1–10.
27. Jagota, A., and Dawson, P. R. (1988). Micromechanical modeling of powder compacts—I. Unit problems for sintering and traction-induced deformation. *Acta Metall.* **36**: 2551–2561.
28. Jagota, A., and Dawson, P. R. (1990). Simulation of viscous sintering of two particles. *J. Am. Ceram. Soc.* **73**: 173–177.
29. Jagota, A. (1994). Simulation of the viscous sintering of coated particles. *J. Am. Ceram. Soc.* **77**: 2237–2239.
30. Ashby, M. F. (1974). A first report on sintering diagrams. *Acta Metall.* **22**: 275–289.
31. Swinkels, F. B., and Ashby, M. F. (1981). A second report on sintering diagrams. *Acta Metall.* **29**: 259–281.

32. Gregg, R. A., and Rhines, F. N. (1973). Surface tension and the sintering force in copper. *Metall. Trans.* 4: 1365–1374.
33. De Jonghe, L. C., and Rahaman, M. N. (1984). A loading dilatometer. *Rev. Sci. Instrum.* 55: 2007–2010.
34. Rahaman, M. N., De Jonghe, L. C., and Brook, R. J. (1986). Effect of shear stress on sintering. *J. Am. Ceram. Soc.* 69: 53–58.
35. Rahaman, M. N., and De Jonghe, L. C. (1987). Creep-sintering of ZnO. *J. Mater. Sci.* 22: 4326–4330.
36. Chu, M.-Y., De Jonghe, L. C., and Rahaman, M. N. (1989). Effect of temperature on the densification/creep viscosity during sintering. *Acta Metall.* 37: 1415–1420.
37. Rahaman, M. N., De Jonghe, L. C., and Chu, M.-Y. (1991). Effect of green density on densification and creep during sintering. *J. Am. Ceram. Soc.* 74: 514–519.
38. Venkatachari, K. R., and Raj, R. (1986). Shear deformation and densification of powder compacts. *J. Am. Ceram. Soc.* 69: 499–506.
39. Aigeltinger, E. H. (1975). Relating microstructure and sintering force. *Int. J. Powder Met. Powder Technol.* **11**: 195–203.
40. Beere, W. (1975). A unifying theory of the stability of penetrating liquid phases and sintering pores. *Acta Metall.* **23**: 131–138.
41. Vieira, J. M., and Brook, R. J. (1984). Kinetics of hot-pressing: the semi-logarithmic law. *J. Am. Ceram. Soc.* 67: 245–249.
42. Atkinson, H. V. (1988). Theories of normal grain growth in pure single phase systems. *Acta Metall.* 36: 469–491.
43. Burke, J. E., and Turnbull, D. (1952). *Progr. Metal Phys.* 3: 220.
44. Feltham, P. (1957). Grain growth in metals. *Acta Metall.* 5: 97–105.
45. Hillert, M. (1965). On the theory of normal and abnormal grain growth. *Acta Metall.* 13: 227–238.
46. Louat, N. P. (1974). On the theory of normal grain growth. *Acta Metall.* **22**: 721–724.
47. Hunderi, O., and Ryun, N. (1980). The kinetics of normal grain growth. *J. Mater. Sci.* 15: 1104–1108.
48. Smith, C. S. (1948). Grains, phases, and interfaces: an interpretation of microstructure. *Trans. AIME* 175: 15–51.
49. Smith, C. S. (1952). Grain shapes and other metallurgical applications of topology, *Metal Interfaces*, pp. 65–113, Cleveland, OH: ASM.
50. Rhines, F. N., and Craig, K. R. (1974). Mechanism of steady-state grain growth in aluminum. *Metall. Trans.* 5: 413–425.
51. Anderson, M. P., Srolovitz, D. J., Grest, G. S., and Sahni, P. S. (1984). Computer simulation of grain growth—I. Kinetics. *Acta Metall.* **32**: 783–791.
52. Srolovitz, D. J., Anderson, M. P., Sahni, P. S., and Grest, G. S. (1984). Computer simulation of grain growth—II. Grain size distribution, topology, and local dynamics. *Acta Metall.* 32: 793–802.
53. Brook, R. J. (1976). Controlled grain growth, *Treatise on Materials Science and Technology*, pp. 331–364, Wang, F. F. Y., ed., New York: Academic Press.
54. Chol, G. R. (1971). Influence of milled powder particle size distribution on the microstructure and electrical properties of sintered Mn–Zn ferrites. *J. Am. Ceram. Soc.* 54: 34–39.
55. Monahan, R. D., and Halloran, J. W. (1979). Single crystal boundary migration in hot-pressed aluminum oxide. *J. Am. Ceram. Soc.* **62**: 564–567.
56. Rios, P. R. (1992). Abnormal grain growth in pure materials. *Acta Metall.* 40: 2765–2768.
57. Rios, P. R. (1994). Abnormal grain growth in materials containing particles. *Acta Metall.* **42**: 839–843.

58. Srolovitz, D. J., Grest, G. S., and Anderson, M. P. (1985). Computer simulation of grain growth—II. Grain size distribution, topology, and local dynamics. *Acta Metall.* 33: 2233–2247.
59. Thompson, C. V., Frost, H. J., and Spaepen, F. (1987). The relative rates of secondary and normal grain growth. *Acta Metall.* 35: 887–890.
60. Rollet, A. D., Srolovitz, D. J., and Anderson, M. P. (1989). Simulation and theory of abnormal grain growth—anisotropic grain boundary energies and mobilities. *Acta Metall.* 37: 1227–1240.
61. Yang, W., Chen, L., and Messing, G. L. (1995). Computer simulation of anisotropic grain growth. *Mater. Sci. Eng. A* 195: 179–185.
62. Kunaver, U., and Kolar, D. Three-dimensional computer simulation of anisotropic grain growth in ceramics. *Acta Mater.* 46: 4629–4640.
63. Harmer, M. P. (1990). A history of the role of MgO in the sintering of α-Al_2O_3. *Ceram. Trans.* 7: 13–49.
64. Berry, K. A., and Harmer, M. P. (1986). Effect of MgO solute on microstructure development in Al_2O_3. *J. Am. Ceram. Soc.* 69: 143–149.
65. Handwerker, C. A., Dynys, J. M., Cannon, R. M., and Coble, R. L. (1990). Dihedral angles in magnesia and alumina: distributions from surface thermal grooves. *J. Am. Ceram. Soc.* 73: 1371–1377.
66. Kaysser, W. A., Sprissler, M., Handwerker, C. A., and Blendell, J. E. (1987). Effect of liquid phase on the morphology of grain growth in alumina. *J. Am. Ceram. Soc.* 70: 339–343.
67. Song, H., and Coble, R. L. (1990). Origin and growth kinetics of platelike abnormal grains in liquid-phase-sintered alumina. *J. Am. Ceram. Soc.* 73: 2077–2085.
68. Horn, D. S., and Messing, G. L. (1995). Anisotropic grain growth in TiO_2-doped alumina. *Mater. Sci. Eng. A* 195: 169–178.
69. Powers, J. D., and Glaeser, A. M. (1996). Titanium effects on sintering and grain growth of alumina, *Sintering Technology*, pp. 333–340, German, R. M., Messing, G. L., and Cornwall, R. M., eds., New York: Marcel Dekker.
70. Becher, P. F. (1991). Microstructural design of toughened ceramics. *J. Am. Ceram. Soc.* 74: 255–269.
71. Cao, J. J., Moberly-Chan, J. J., De Jonghe, L. C., Gilbert, C. J., and Ritchie, R. O. (1996). In situ toughened silicon carbide with Al–B–C additions. *J. Am. Ceram. Soc.* 79: 461–469.
72. Huang, T., Rahaman, M. N., Mah, T.-I., and Parthasarathay, T. A. (2000). Effect of SiO_2 and Y_2O_3 additives on the anisotropic grain growth of dense mullite. *J. Mater. Res.* 15: 718–726.
73. Seabaugh, M. M., Kerscht, I. H., and Messing G. L. (1997). Texture development by templated grain growth in liquid-phase-sintered α-alumina. *J. Am. Ceram. Soc.* 80: 1181–1188.
74. Horn, J. A., Zhang, S. C., Selvaraj, U., Messing, G. L., and Trolier-McKinstry, S. (1999). Templated grain growth of textured bismuth titanate. *J. Am. Ceram. Soc.* 82: 921–926.
75. Patwardhan, J. S. (2000). Texture and grain alignment in piezoelectric bismuth titanate ceramics, MS Thesis, University of Missouri-Rolla, Rolla, MO.
76. Yamamoto, T., and Sakuma, T. (1994). Fabrication of barium titanate single crystals by solid state grain growth. *J. Am. Ceram. Soc.* 77: 1107–1109.
77. Li, T., Scotch, A. M., Chan, H. M., Harmer, M. P., Park, S., and Shrout, T. R. (1998). Single crystals of $Pb(Mg_{1/3}Nb_{2/3})O_3$-35 mol% $PbTiO_3$ from polycrystalline precursors. *J. Am. Ceram. Soc.* 81: 244–248.
78. Greenwood, G. W. (1956). The growth of dispersed precipitates in solutions. *Acta Metall.* 4: 243–248.
79. Lifshitsz, I. M., and Slyozov, V. V. (1961). The kinetics of precipitation from supersaturated solutions. *Phys. Chem. Solids* 19: 35–50.

80. Wagner, C. (1961). Theory of Ostwald ripening. *Z. Electrochem.* 65: 581–591.
81. Fischmeister, H., and Grimvall, G. (1973). Ostwald ripening—a survey. *Mater. Sci. Res.* 6: 119–149.
82. Ardell, A. J. (1972). The effect of volume fraction on particle coarsening: theoretical considerations. *Acta Metall.* 20: 61–71.
83. Enomoto, Y., Kawasaki, K., and Tokuyama, M. (1987). Computer modeling of Ostwald ripening. *Acta Metall.* 35: 904–913.
84. Enomoto, Y., Kawasaki, K., and Tokuyama, M. (1987). The time dependent behavior of the Ostwald ripening for the finite volume fraction. *Acta Metall.* 35: 915–922.
85. Kingery, W. D. (1974). Plausible concepts necessary and sufficient for interpretation of ceramic grain boundary phenomena: I, grain-boundary characteristics, structure and electrostatic potential. *J. Am. Ceram. Soc.* 57: 1–8.
86. Kingery, W. D. (1974). Plausible concepts necessary and sufficient for interpretation of ceramic grain boundary phenomena: II, solute segregation, grain boundary diffusion, and general discussion. *J. Am. Ceram. Soc.* 57: 74–83.
87. Chiang, Y.-M., Henriksen, A. F., Finello, D., and Kingery, W. D. (1981). *J. Am. Ceram. Soc.* 64: 383.
88. Ikeda, J. A. S., and Chiang, Y.-M. (1993). Space charge segregation at grain boundaries in titanium dioxide: I, relationship between lattice defect chemistry and space charge potential. *J. Am. Ceram. Soc.* 76: 2437–2446.
89. Ikeda, J. A. S., Chiang, Y.-M., Garratt-Reed, A. J., and Vander Sande, J. B. (1993). Space charge segregation at grain boundaries in titanium dioxide: II, model experiments. *J. Am. Ceram. Soc.* 76: 2447–2459.
90. Cahn, J. W. (1962). The impurity drag effect in grain boundary motion. *Acta Metall.* 10: 789–798.
91. Chen, P.-L., and Chen, I.-W. (1994). Role of defect interaction in boundary mobility and cation diffusivity of CeO_2. *J. Am. Ceram. Soc.* 77: 2289–2297.
92. Rahaman, M. N., and Zhou, Y.-C. (1995). Effect of dopants on the sintering of ultra-fine CeO_2 powder. *J. Eur. Ceram. Soc.* 15: 939–950.
93. Coble, R. L. (1962). Transparent alumina and method of preparation, US Patent # 3, 026, 210.
94. Brook, R. J., Tuan, W. H., and Xue, L. A. (1988). Critical issues and future directions in sintering science. *Ceram. Trans.* 1B: 811–823.
95. Rahaman, M. N., and Manalert, R. (1998). Grain boundary mobility of $BaTiO_3$ doped with aliovalent cations. *J. Eur. Ceram. Soc.* 18: 1063–1071.
96. Rahaman, M. N., De Jonghe, L. C., Voight, J. A., and Tuttle, B. A. (1990). Low temperature sintering of zinc oxide varistors. *J. Mater. Sci.* 25: 737–742.
97. Jorgensen, P. J., and Anderson, R. C. (1967). Grain-boundary segregation and final-stage sintering of Y_2O_3. *J. Am. Ceram. Soc.* 50: 553–558.
98. Prochazka, S., and Scanlan, R. M. (1975). Effect of boron and carbon on sintering of SiC. *J. Am. Ceram. Soc.* 58: 72.
99. Yan, M. F., Cannon, R. M., and Bowen, H. K. (1977). Grain boundary migration in ceramics, *Ceramic Microstructures '76*, pp. 276–307, Fulrath, R. M., and Pask, J. A., eds., Boulder, CO: Westview Press.
100. Glaeser, A. M., Bowen, H. K., and Cannon, R. M. (1986). Grain-boundary migration in LiF: I, mobility measurements. *J. Am. Ceram. Soc.* 69: 119–125.
101. Lange, F. F., and Hirlinger, M. M. (1984). Hindrance of grain growth in Al_2O_3 by ZrO_2 inclusions. *J. Am. Ceram. Soc.* 67: 164–168.
102. Stearns, L. C., and Harmer, M. P. (1996). Particle-inhibited grain growth in Al_2O_3-SiC: I, experimental results. *J. Am. Ceram. Soc.* 79: 3013–3019.

103. Stearns, L. C., and Harmer, M. P. (1996). Particle-inhibited grain growth in Al_2O_3-SiC: II, equilibrium and kinetic analyses. *J. Am. Ceram. Soc.* 79: 3020–3028.
104. Greskovich, C., and Lay, K. W. (1972). Grain growth in very porous Al_2O_3 compacts. *J. Am. Ceram. Soc.* 55: 142–146.
105. Rhines, F., and DeHoff, R. (1983). Channel network decay in sintering. *Mater. Sci. Res.* 16: 49–61.
106. Coleman, S. C., and Beeré, W. B. (1975). The sintering of open and closed porosity in UO_2. *Philos. Mag.* **31**: 1403–1413.
107. Shewmon, P. G. (1964). *Trans. AIME* **230**: 1134.
108. Hsueh, C. H., Evans, A. G., and Coble, R. L. (1982). Microstructure development during final/initial stage sintering: I, pore/grain boundary separation. *Acta Metall.* 30: 1269–1279.
109. Brook, R. J. (1969). Pore–grain boundary interactions and grain growth. *J. Am. Ceram. Soc.* 52: 56–57.
110. Berry, K. A., and Harmer, M. P. (1986). Effect of MgO solute on microstructure development in Al_2O_3. *J. Am. Ceram. Soc.* 69: 143–149.
111. Handwerker, C. A., Cannon, R. M., and Coble, R. L. (1984). Final stage sintering of MgO. *Adv. Ceram.* **10**: 619–631.
112. Carpay, F. M. A. (1977). Discontinuous grain growth and pore drag. *J. Am. Ceram. Soc.* 60: 82–83.
113. Kim, H. Y., Lee, J.-A., and Kim, J. J. (2000). Densification behavior of fine alumina and coarse alumina compacts during liquid phase sintering with the addition of talc. *J. Am. Ceram. Soc.* 83: 3128–3134.
114. Elfwing, M., Osterlund, R., and Olsson, E. (2000). Differences in wetting characteristics of Bi_2O_3 polymorphs in ZnO Varistor Materials. *J. Am. Ceram. Soc.* 83: 2311–2314.
115. Kim, D.-H., and Kim, C. H. (1990). Toughening behavior of silicon carbide with additions of yttria and alumina. *J. Am. Ceram. Soc.* 73: 1431–1434.
116. Terwilliger, G. F., and Lange, F. F. (1975). Pressureless sintering of silicon nitride. *J. Mater. Sci.* **10**: 1169–1174.
117. Riley, F. L. (2000). Silicon nitride and related materials. *J. Am. Ceram. Soc.* 83: 245–265.
118. Rhim, S. M., Bak, H., Hong, S., Kim, O. K. (2000). Effects of heating rate on the sintering behavior and the dielectric properties of $Ba_{0.7}Sr_{0.3}TiO_3$ ceramics prepared by boron-containing liquid-phase sintering. *J. Am. Ceram. Soc.* **83**: 3009–3013.
119. Luo, J., Wang, H., and Chiang, Y.-M. (1999). Origin of solid-state activated sintering in Bi_2O_3-doped ZnO. *J. Am. Ceram. Soc.* **82**: 916.
120. Wu, S. J., De Jonghe, L. C., and Rahaman, M. N. (1985). Subeutectic densification and second phase formation in Al_2O_3–CaO. *J. Am. Ceram. Soc.* 68: 385–388.
121. German, R. M. (1984). *Powder Metallurgy Science*, p. 182, Princeton, NJ: Metal Powder Industries Federation.
122. Zhang, X. F., Sixta, M., and De Jonghe, L. C. (2000). Grain boundary evolution in hot-pressed ABC–SiC. *J. Am. Ceram. Soc.* 83: 2813–2820.
123. Kwon, O. J., and Yoon, D. N. (1981). Closure of isolated pores in liquid phase sintering of W–Ni. *Int. J. Powder Technol.* **17**: 127–133.
124. Shaw, T. M. (1986). Liquid redistribution during liquid phase sintering. *J. Am. Ceram. Soc.* 69: 27–34.
125. Gu, H., Pan, X. Q., Cannon, R. M., and Ruhle, M. (1998). Dopant distribution in grain-boundary films in calcia-doped silicon nitride ceramics. *J. Am. Ceram. Soc.* **81**: 3125–3135.
126. Brydson, R., Chen, S.-C., Riley, F. L., Milne, S. J., Pan, X., and Rühle, M. (1998). Microstructure and chemistry of intergranular glassy films in liquid-phase-sintered alumina. *J. Am. Ceram. Soc.* **81**: 369–379.

127. Buist, D. S., Jackson, B., Stephenson, I. M., Ford, W. F., and White, J. (1965). The kinetics of grain growth in two-phase (solid–liquid) systems. *Trans. Br. Ceram. Soc.* **64**: 173–209.
128. Kapolnek, S., and De Jonghe, L. C. (1991). Particulate composites from coated powders. *J. Eur. Ceram. Soc.* 7: 345–351.
129. Norton, F. H. (1974). *Elements of Ceramics*, Reading, MA: Addison-Wesley.
130. Lange, F. F. (1982). Liquid phase sintering: are liquids squeezed out from between compressed particles? *J. Am. Ceram. Soc.* **65**: C23.
131. Clarke, D. R., Shaw, T. M., Phillips, A. P., and Horn, R. G. (1993). Possible electrical double layer contribution of the equilibrium thickness of intergranular glass films in polycrystalline ceramics. *J. Am. Ceram. Soc.* **76**: 1201–1204.
132. Wang, H., and Chiang, Y.-M. (1998). Thermodynamic stability of intergranular amorphous films in bismuth-doped zinc oxide. *J. Am. Ceram. Soc.* **81**: 89–96.
133. Tanaka, I., Kleebe, H.-J, Cinibulk, M., Bruley, J., Clarke, D., and Ruhle, M. (1994). Calcium concentration dependence of the intergranular film thickness in silicon nitride. *J. Am. Ceram. Soc.* 77: 911–914.
134. Wu, T. H. (1976). *Soil Mechanics*, Boston, MA: Allyn and Bacon, Inc.
135. Bridgewater, J. (1994). Mixing and segregation in particle flow, *Granular Matter, An Interdisciplinary Approach*, Metha, A., ed., New York: Springer-Verlag.
136. Clarke, D. R. (1987). On the equilibrium thickness of intergranular glass phases in ceramic materials. *J. Am. Ceram. Soc.* **70**: 15–22.
137. Lee, S.-M., Chaix, J.-M., Martin, C. L., Allibert, C. H., and Kang, S. J. (1999). Computer simulation of particle rearrangement in the presence of liquid. *Met. Mater.* 5: 197–204.
138. Morey, G. W. (1938). *Properties of Glass*, p. 211, New York: Reinhold Publ. Co.
139. Mills, K. C., and Keene, B. J. (1987). Physical properties of BOS slags. *Int. Mater. Rev.* **32**: 1–120.
140. Cannon, R. M., Saiz, E., Tomsia, A. P., and Carter, W. C. (1995). Reactive wetting taxonomy. *Mat. Res. Soc. Symp. Proc.* **357**: 279–292.
141. Huang, K. S., German, R. M., and Lenel, F. V. (1986). Capillary forces in the early stages of liquid phase sintering. *Rev. Powder Metall. Phys. Ceram.* 3: 113–164.
142. Carter, W. C. (1996). Surface evolver as a tool for materials science research, *Mathematics of Microstructural Evolution*, Chen, L., Fulz, B., Cahn, J., Manning, J., Morral, J., and Simmons, J., eds., Warrendale, PA: TMS.
143. Cambier, F., and Leriche, A. (1996). Vitrification, *Materials Science and Technology*, Vol. 17B, pp. 123–144, Cahn, R. W., Haasen, P., and Kramer, E. J., eds., New York: VCH.
144. Bergeron, C. G., and Risbud, S. H. (1984). *Introduction to Phase Equilibria in Ceramics*, Columbus, OH: American Ceramic Soc.
145. De Jonghe, L. C., and Goo, E. (1978). Transient eutectics in sintering of sodium beta alumina, *Processing of Crystalline Ceramics*, pp. 433–441, Palmour III, H., Davis, R. F., and Hare, R. T., eds., New York: Plenum Press.
146. Chick, L. A., Liu, J., Stevenson, J. W., Armstrong, T. R., McCready, D. E., Maupin, G. D., Coffey, G. W., and Coyle, C. A. (1997). Phase transitions and transient liquid-phase sintering in calcium-substituted lanthanum chromite. *J. Am. Ceram. Soc.* **80**: 2109–2120.
147. Yangyun, S., and Brook, R. J. (1985). Preparation of zirconia toughened ceramics by reaction sintering. *Sci. Sintering* **17**: 35–47.
148. Jack, K. H., and Wilson, W. I. (1972). *Nat. Phys. Sci.* **238**: 28–34.
149. Bartsch, M., Saruhan, B., Schmucker, M., and Schneider, H. (1999). Novel low-temperature processing route of dense mullite ceramics by reaction sintering of amorphous SiO_2-coated gamma-Al_2O_3 particle nanocomposites. *J. Am. Ceram. Soc.* **82**: 1388–1392.
150. Leblud, C., Anseau, M. R., di Rupo, E., Cambier, F., and Fierens, P. (1981). Reaction sintering of $ZnO–Al_2O_3$ mixtures. *J. Mater. Sci. Lett.* **16**: 539–544.

151. Sacks, M. D., Bozkurt, N., and Scheiffele, G. (1991). Fabrication of mullite and mullite–matrix composites by transient viscous sintering of composite powders. *J. Am. Ceram. Soc.* 74: 2428–2437.
152. Claussen, N., and Jahn, J. (1980). Mechanical properties of sintered, in situ-reacted mullite–zirconia composites. *J. Am. Ceram. Soc.* 63: 228–229.
153. Koga, N., and Criado, J. M. (1998). Kinetic analyses of solid-state reactions with a particle size distribution. *J. Am. Ceram. Soc.* 81: 2901–2909.
154. Hulbert, S. F., and Popovich, M. J. (1969). Kinetics and mechanisms of the reaction between TiO_2 and $SrCO_3$. *Mater. Sci. Res.* 4: 442.
155. Rahaman, M. N., and De Jonghe, L. C. (1993). Reaction sintering of zinc ferrite during constant rates of heating. *J. Am. Ceram. Soc.* 76: 1739–1744.
156. Hong, W. S., De Jonghe, L. C., Yang, X., and Rahaman. M. N. (1995). Reaction sintering of $ZnO–Al_2O_3$. *J. Am. Ceram. Soc.* 78: 3217–3224.
157. Evans, A. G. (1982). Considerations of inhomogeneity effects in sintering. *J. Am. Ceram. Soc.* 65: 497–501.
158. Scherer, G. W. (1987). Sintering with rigid inclusions. *J. Am. Ceram. Soc.* 70: 719–725.
159. Raj, R., and Bordia, R. K. (1984). Sintering behavior of bimodal powder compacts. *Acta Metall.* 32: 1003–1019.
160. Hsueh, C.-H., Evans, A. G., Cannon, R. M., and Brook, R. J. (1986). Viscoelastic stresses and sintering damage in heterogeneous powder compacts. *Acta Metall.* 34: 927–936.
161. Bordia, R. K., and Scherer, G. W. (1988). On constrained sintering: parts 1, 2, and 3. *Acta Metall.* 36: 2393–2416.
162. Sudre, O., Bao, G., Fan, B., Lange, F. F., and Evans, A. G. (1992). Effect of inclusions on densification: II, numerical model. *J. Am. Ceram. Soc.* 75: 525–531.
163. Hu, C.-H., and Rahaman, M. N. (1992). Factors controlling the sintering of ceramic particulate composites: II, coated inclusion particles. *J. Am. Ceram. Soc.* 75: 2066–2070.
164. Scherer, G. W., and Garino, T. J. (1985). Viscous sintering on a rigid substrate. *J. Am. Ceram. Soc.* 68: 216–220.
165. Hu, M., Thouless, M., and Evans, A. G. (1988). The decohesion of thin films from brittle substrates. *Acta Metall.* 36: 1301–1308.
166. Kueper, T. W. (1992). Sol–Gel ceramic electrolyte films on porous substrates, PhD Thesis, University of California, Berkeley, CA.
167. Miller, K. T., Lange, F. F., and Marshall, D. B. (1990). The instability of polycrystalline films: experiment and theory. *J. Mater. Res.* 5: 151–157.
168. Anderson, H. U. (1974). Influence of oxygen activity on the sintering of $MgCr_2O_4$. *J. Am. Ceram. Soc.* 57: 34–37.
169. Hwang, S.-L., Becher, P. F., and Lin, H.-T. (1997). Desintering process in the gas-pressure sintering of silicon nitride. *J. Am. Ceram. Soc.* 80: 329–335.
170. Coble, R. L. (1962). Sintering of alumina: effect of atmosphere. *J. Am. Ceram. Soc.* 45: 123–127.
171. Snow, G. S. (1973). Improvements in atmosphere sintering of transparent PLZT ceramics. *J. Am. Ceram. Soc.* 56: 479–480.
172. Woolfrey, J. L., and Bannister, M. J. (1972). Nonisothermal sintering techniques for studying initial stage sintering. *J. Am. Ceram. Soc.* 55: 390–397.
173. Boccaccini, A. R., Stumpfe, W., Taplin, D. M. R., and Ponton, C. B. (1996). Densification and crystallization of glass powder compacts during constant heating rate sintering. *Mater. Sci. Eng. A* 219: 26–31.
174. Chu, M-Y., Rahaman, M. N., and Brook, R. J. (1991). Effect of heating rate on sintering and coarsening. *J. Am. Ceram. Soc.* 74: 1217–1225.

175. Lange, F. F. (1989). Approach to reliable powder processing, *Ceramic Trans.*, 1, *Ceramic Powder Science IIB*, pp. 1069–1083, Messing, G. L., Fuller, E. R., and Hausner, H., eds., American Ceramic Society. Westerville, OH.
176. Duncan, J. H., and Budgen, W. G. (1981). Two-peak firing of beta-alumina. *Proc. Br. Ceram. Soc.* **31**: 221–228.
177. Lin, F. J. T., De Jonghe, L. C., and Rahaman, M. N. (1997). Microstructure refinement of sintered alumina by a two-step sintering technique. *J. Am. Ceram. Soc.* **80**: 2269–2278.
178. Chu, M.-Y., De Jonghe, L. C., Lin, M. F. K., and Lin, F. J. T. (1991). Pre-coarsening to improve microstructure and sintering of powder compacts. *J. Am. Ceram. Soc.* **74**: 2902–2911.
179. Huckabee, M. L., Hare, T. M., and Palmour III, H. (1978). Rate controlled sintering as a processing methods, *Processing of Crystalline Ceramics*, pp. 205–215, Palmour III, H., Davis, R. F., and Hare, R. T., eds., New York: Plenum Press.
180. Huckabee, M. L., Paisley, M. J., Russell, R. L., and Palmour III, H. (1994). RCS-taking the mystery out of densification profiles. *J. Am. Ceram. Soc.* **73**: 82–89.
181. Agarwal, G., Speyer, R. F., and Hackenberger, W. S. (1996). Microstructural development of ZnO using a rate-controlled sintering dilatometer. *J. Mat. Res.* **11**: 671–678.
182. Ragulya, A. V. (1998). Rate-controlled synthesis and sintering of nanocrystalline barium titanate powder. *Nanostruct. Mater.* **10**: 349–355.
183. Pickup, H., Eisele, U., Gilbart, E., and Brook, R. J. (1985). Analysis of coarsening and densification kinetics during the heat treatment of nitrogen ceramics, *Non-Oxide Technical and Engineering Ceramics*, pp. 41–51, Hampshire, S., ed., New York: Elsevier Applied Science.
184. Brook, R. J. (1982). Fabrication principles for the production of ceramics with superior mechanical properties. *Proc. Br. Ceram. Soc.* **32**: 7–15.
185. Johnson, D. L. (1984). Ultra-rapid Sintering. *Mater. Sci. Res.* **10**: 243–247.
186. Fang, Y., Agrawal, D. K., Roy, D., and Roy, R. (1994). Microwave sintering of hydroxyapatite ceramics. *J. Mater. Res.* **9**: 180–189.
187. Birnboim, A., and Carmel, Y. (1999). Simulation of microwave sintering of ceramic bodies with complex geometry. *J. Am. Ceram. Soc.* **82**: 3024–3033.
188. Birnboim, A. *et al.* (1998). Comparative study of microwave sintering of zinc oxide at 2.45, 30, and 83 GHz. *J. Am. Ceram. Soc.* **81**: 1493–2001.
189. Cheng, J., Agrawal, D., Roy, R., and Jayan, P. S. (2000). Continuous microwave sintering of alumina abrasive grits. *J. Mater. Process. Technol.* **108**: 26–32.
190. Henrichsen, M., Hwang, J., Dravid, V. P., and Johnson, D. L. (2000). Ultrarapid phase conversion in beta-alumina tubes. *J. Am. Ceram. Soc.* **83**: 2861–2869.
191. Gao, L., Shen, Z., Miyamoto, H., and Nygren, M. (1999). Superfast densification of oxide/oxide ceramic composites. *J. Am. Ceram. Soc.* **82**: 1061–1069.
192. Takeuchi, T., Tabuchi, M., and Kageyama, H. (1999). Preparation of dense $BaTiO_3$ ceramics with submicrometer grains by spark plasma sintering. *J. Am. Ceram.* **82**: 939–943.
193. Gutmanas, E., and Gotman, I. (1999). Dense high-temperature ceramics by thermal explosion under pressure. *J. Eur. Ceram. Soc.* **19**: 2381–2390.
194. Vasilos, T., and Spriggs, R. M. (1966). Pressure sintering of ceramics, *Progress in Ceramic Science*, Vol. 4, pp. 97–107, Burke, J., ed., New York: Pergamon Press.
195. POCO Graphite Inc, P.O. Box 2121, Decatur, TX 76234, USA.
196. Carborundum Boron Nitride, 168 Creekside Drive, Amherst, NY 14228, USA.
197. Lange, F. F., and Terwilliger, G. R. (1973). The powder vehicle hot-pressing technique. *Bull. Am. Ceram. Soc.* **52**: 563–569.
198. Rigby, F. (1981). Development of hot pressing techniques at Springfields Nuclear Laboratories. *Proc. Br. Ceram. Soc.* **31**: 249–257.

199. Wilkinson, D. S., and Ashby, M. F. (1975). The development of pressure sintering maps. *Mater. Sci. Res.* Vol. 10, *Sintering and Catalysis*, pp. 473–478, Kuczynski, G., ed., New York: Plenum Press.
200. Zhang, G.-J., Deng, Z.-Y., Kondo, N., Yang, J.-F., Ohji, and T. (2000). Reactive hot pressing of ZrB_2–SiC composites. *J. Am. Ceram. Soc.* **83**: 2330–2338.
201. Wen, G., Li, S. B., Zhang, B. S., and Guo, Z. X. (2000). Processing of *in situ* toughened B–W–C composites by reaction hot pressing of B_4C and WC. *Scripta Mater.* **43**: 853–858.
202. Hosoi, K., Hashida, T., Takahashi, H., Yamasaki, N., and Korenaga, T. (1996). New processing technique for hydroxyapatite ceramics by the hydrothermal hot-pressing method. *J. Am. Ceram. Soc.* 79: 2771–2779.
203. Yanagisawa, K., Ioku, K., and Yamasaki, N. (1997). Formation of anatase porous ceramics by hydrothermal hot-pressing of amorphous titania spheres. *J. Am. Ceram. Soc.* **80**: 1303–1306.
204. He, Y. J., Winnubst, A. J. A., Verweij, A., and Burggraaf, A. J. (1994). Sinter-forging of zirconia toughened alumina. *J. Mater. Sci.* 29: 6505–6512.
205. Kondo, N., Suzuki, Y., and Ohji, T. (1999). Superplastic sinter-forging of silicon nitride with anisotropic microstructure formation. *J. Am. Ceram. Soc.* **82**: 1067–1073.
206. Saller, H., Paprocki, S., Dayton, R., and Hodge, E. (1964). A method of bonding. Can. Patent # 680160.
207. Zhou, Y.-C., and Rahaman, M. N. (1993). Hydrothermal synthesis and sintering of ultra-fine CeO_2 powders. *J. Mater. Res.* **8**: 1680–1686.
208. Rahaman, M. N., and Zhou, Y.-C. (1995). Effect of dopants on the sintering of ultra-fine CeO_2 powder. *J. Eur. Ceram. Soc.* **15**: 939–950.
209. Coble, R. L. (1973). Effects of particle size distribution in initial stage sintering. *J. Am. Ceram. Soc.* **56**: 461–466.
210. Onoda, G. Y., and Messing, G. L. (1978). Packing and sintering relations for binary powders. *Mater. Sci. Res.* **11**: 99–122.
211. Smith, J. P., and Messing, G. L. (1984). Sintering of bimodally distributed alumina powders. *J. Am. Ceram. Soc.* 67: 238–242.
212. Patterson, B. R., and Benson, L. A. (1983). The effect of powder size distribution on sintering. *Progr. Powder Met.* **39**: 215–230.
213. German, R. M. (1992). Sintering densification for powder mixtures of varying distribution widths. *Acta Metall. Mater.* **40**: 2085–2089.
214. Chapell, J. S., Ring, T. A., and Birchall, J. D. (1986). Particle size distribution effects on sintering rates. *J. Appl. Phys.* **60**: 383–391.
215. Yamaguchi T., and Kosha, H. (1981). Sintering of acicular Fe_2O_3 particles. *J. Am. Ceram. Soc.* 64: C84–C85.
216. Mikijelj, B., and Whittemore, O. J. (1987). Grain cuboidization during sintering of MgO–$MgCl_2$ (1%). *Am. Ceram. Soc. Bull.* 66: 809–812.
217. Kumar, P., and Johnson, D. L. (1974). Sintering of CoO. *J. Am. Ceram. Soc.* 57: 62–64.
218. Thompson, R. J., and Munir, Z. A. (1982). Influence of particle size on the sintering kinetics of ultrapure sodium chloride. *J. Am. Ceram. Soc.* 65: 312–316.
219. Wang, Z. Y., Harmer, M. P., and Chou, Y. T. (1986). Pore-boundary configurations in lithium fluoride. *J. Am. Ceram. Soc.* 69: 735–740.
220. Slamovich, E. B., and Lange, F. F. (1990). Densification behavior of single-crystal and polycrystalline spherical particles of zirconia. *J. Am. Ceram. Soc.* 73: 3368–3375.
221. Edelson, L. H., and Glaeser, A. M. (1988). Role of particle substructure in the sintering of monosized titania. *J. Am. Ceram. Soc.* 71: 225–235.
222. Edelson, L. H., and Glaeser, A. M. (1988). Effects of thermal pretreatment on coarsening of nominally monodispersed titania. *J. Am. Ceram. Soc.* 71: C198–C201.

223. Rhodes, W. W. (1981). Agglomerate and particle size effects on sintering of yttria-stabilized zirconia. *J. Am. Ceram. Soc.* **64**: 19–22.
224. Barringer, E. A., and Bowen, H. K. (1982). Formation, packing, and sintering of monodisperse TiO_2 powders. *J. Am. Ceram. Soc.* **65**: C199–C201.
225. Barringer, E. A., and Bowen, H. K. (1988). Effect of particle packing on the sintered microstructure. *Appl. Phys. A* **45**: 271–275.
226. Liniger, E., and Raj, R. (1987). Packing and sintering of two-dimensional structures made from bimodal particle size distributions. *J. Am. Ceram. Soc.* **70**: 843–849.
227. Yeh, T. S., and Sacks, M. D. (1990). Effect of green microstructure on sintering of alumina. *Ceram. Trans.* **7**: 309–331.
228. Cesarano III, J., and Aksay, I. A. (1988). Processing of highly concentrated aqueous α-alumina suspensions stabilized with polyelectrolytes. *J. Am. Ceram. Soc.* **71**: 1062–1067.
229. Weiser, M. W., and De Jonghe, L. C. (1986). Rearrangement during sintering in two-dimensional arrays. *J. Am. Ceram. Soc.* **69**: 822–826.
230. Exner, H. E. (1979). Principles of single phase sintering. *Rev. Powder Metall. Phys. Ceram.* **1**: 1–251.
231. Lange, F. F. (1984). Sinterability of agglomerated powders. *J. Am. Ceram. Soc.* **67**: 83–89.
232. Lin, M., De Jonghe, L. C., and Rahaman, M. N. (1987). Creep-sintering of MgO powder compacts. *J. Am. Ceram. Soc.* **70**: 360–366.
233. Harmer, M. P., and Zhao, J. (1987). Effect of pores on microstructure development, *Ceramic Micorstructures '86, Mater. Sci. Res.*, Vol. 21, pp. 455–464, Pask, J. A., and Evans, A. G., eds., New York: Plenum Press.
234. Chen, P. L., and Chen, I.-W. (1997). Sintering of fine oxide powders: II, sintering mechanisms. *J. Am. Ceram. Soc.* **80**: 637–645.
235. Rahaman, M. N., De Jonghe, L. C., and Chu, M.-Y. (1991). Effect of green density on densification and creep during sintering. *J. Am. Ceram. Soc.* **74**: 514–519.
236. Bruch, C. A. (1962). Sintering kinetics for the high density alumina process. *Am. Ceram. Soc. Bull.* **41**: 799–806.
237. Palmour, H., Geho, M., Russell, R. L., and Hare, T. M. (1992). Study of D_o effects on subsequent densification behavior in spinel and alumina ceramics, *Sintering '91*, pp. 37–44, Chaklader, A. C. D., and Lund, J. A., eds., Brookfield, VT: Trans Tech.
238. Mansour, N. A. L., and White, J. (1963). Causes of residual porosity in sintered uranium dioxide. *Powder Metall.* **6**: 108–121.
239. Occhionero, M. A., and Halloran, J. W. (1984). The influence of green density on sintering, *Mater. Sci. Res.* **16**: 89–102.
240. Bennison, S. J., and Harmer, M. P. (1985). Swelling of hot-pressed alumina. *J. Am. Ceram. Soc.* **68**: 591–597.
241. Readey, D. W. (1990). Vapor transport and sintering. *Ceram. Trans.* **7**: 86–110.
242. Quadir, T., and Readey, D. W. (1989). Microstructure development of zinc oxide in hydrogen. *J. Am. Ceram. Soc.* **72**: 297–302.
243. Lee, J., and Readey, D. W. (1984). Microstructure development of Fe_2O_3 in HCl vapor. *Mater. Sci. Res.* **16**: 145–157.
244. Readey, M. J., and Readey, D. W. (1987). Sintering TiO_2 in HCl atmospheres. *J. Am. Ceram. Soc.* **70**: C358–C361.
245. Thompson, A. M., and Harmer, M. P. (1993). Influence of atmosphere on the final stage sintering kinetics of ultra-high-purity alumina. *J. Am. Ceram. Soc.* **76**: 2248–2256.
246. Anderson, P. J., and Morgan, P. L. (1964). Effect of water vapor on the sintering of MgO. *Trans. Faraday Soc.* **60**: 930–937.
247. Wong, B., and Pask, J. A. (1979). Experimental analysis of sintering of MgO powder compacts. *J. Am. Ceram. Soc.* **62**: 141–146.

248. Northrop, D. A. (1967). Vaporization of lead zirconate-lead titanate materials. *J. Am. Ceram. Soc.* **50**: 441–445.
249. Northrop, D. A. (1968). Vaporization of lead zirconate-lead titanate materials: II, hot-pressed compositions near theoretical density. *J. Am. Ceram. Soc.* **51**: 357–361.
250. Mitomo, M. (1976). Pressure sintering of Si_3N_4. *J. Mater. Sci.* **11**: 1103–1107.
251. Ownby, P. D., and Jungquist, G. E. (1972). Final sintering of Cr_2O_3. *J. Am. Ceram. Soc.* **55**: 433–436.
252. Ownby, P. D. (1973). Oxidation state control of volatile species in sintering. *Mater. Sci. Res.* **6**: 431–437.
253. Anderson, H. U. (1978). Fabrication and property control of $LaCrO_3$ based oxides. *Mater. Sci. Res.* **11**: 469–477.
254. Callister, W. D., Johnson, M. L., Cutler, I. B., and Ure, R. W., Jr. (1979). Sintering chromium oxide with the aid of TiO_2. *J. Am. Ceram. Soc.* **62**: 208–211.
255. Reynolds III, T. (1976). Firing, *Treatise on Materials Science and Technology, Vol. 9*, pp. 199–215, Wang, F. F. Y., ed., New York: Academic Press.
256. Reijnen, P. (1969). Nonstoichiometry and sintering of ionic solids, *Reactivity of Solids*, pp. 99–114, Mitchell, J. W., DeVries, R. C., Roberts, R. W., and Cannon, P., eds., New York: Wiley.
257. Yan, M. F. (1980). Grain growth in Fe_3O_4. *J. Am. Ceram. Soc.* **63**: 443–447.